Title

Microtubule motors transport phagosomes in the RPE, and lack of KLC1 leads to AMD-like pathogenesis

Journal

Journal of Cell Biology, 210(4)

ISSN

0021-9525

Authors

Jiang, Mei
Esteve-Rudd, Julian
Lopes, Vanda S
et al.

Publication Date

2015-08-17

DOI

10.1083/jcb.201410112

Peer reviewed

Microtubule motors transport phagosomes in the RPE, and lack of KLC1 leads to AMD-like pathogenesis

Mei Jiang,[1]* Julian Esteve-Rudd,[1]* Vanda S. Lopes,[1,5] Tanja Diemer,[1] Concepción Lillo,[6] Agrani Rump,[1] and David S. Williams[1,2,3,4,6,7]

[1]Department of Ophthalmology, Jules Stein Eye Institute, [2]Department of Neurobiology, David Geffen School of Medicine, [3]Molecular Biology Institute, and [4]Brain Research Institute, University of California, Los Angeles, Los Angeles, CA 90095
[5]Centre of Ophthalmology, Institute for Biomedical Imaging and Life Sciences, Faculty of Medicine, University Coimbra, 3000-548 Coimbra, Portugal
[6]Department of Pharmacology and [7]Department of Neurosciences, School of Medicine, University of California, San Diego, La Jolla, CA 92093

The degradation of phagosomes, derived from the ingestion of photoreceptor outer segment (POS) disk membranes, is a major role of the retinal pigment epithelium (RPE). Here, POS phagosomes were observed to associate with myosin-7a, and then kinesin-1, as they moved from the apical region of the RPE. Live-cell imaging showed that the phagosomes moved bidirectionally along microtubules in RPE cells, with kinesin-1 light chain 1 (KLC1) remaining associated in both directions and during pauses. Lack of KLC1 did not inhibit phagosome speed, but run length was decreased, and phagosome localization and degradation were impaired. In old mice, lack of KLC1 resulted in RPE pathogenesis that was strikingly comparable to aspects of age-related macular degeneration (AMD), with an excessive accumulation of RPE and sub-RPE deposits, as well as oxidative and inflammatory stress responses. These results elucidate mechanisms of POS phagosome transport in relation to degradation, and demonstrate that defective microtubule motor transport in the RPE leads to phenotypes associated with AMD.

Introduction

The turnover of proteins and organelles is essential for homeostasis and survival of terminally differentiated cells, such as neurons. During this turnover, cells typically synthesize and degrade their own components. However, in an unusual specialization, the turnover of the phototransductive disk membranes that make up the outer segments of vertebrate photoreceptors deviates from this pattern. The photoreceptors synthesize new disk membranes that are added to the base of each outer segment, but to degrade the older disks, at the distal end, they have co-opted the juxtaposed retinal pigment epithelium (RPE) cells. The event begins with phagocytosis of the distal disks by the RPE (Young and Bok, 1969).

The ensuing degradation of the phagocytosed disk membranes by the RPE represents a major metabolic role for these cells. The photoreceptor outer segment (POS) disk membranes are packed very densely (the majority of protein synthesized by a photoreceptor is targeted to the outer segment), and (in mammals) ∼10% of the disks are replaced each day (Young, 1967). Moreover, each RPE cell is responsible for many photoreceptor cells; this number varies among different animals, but, for example, in the central mouse retina, each RPE cell serves over 200 photoreceptor cells (Volland et al., 2015). Thus, the RPE cells are professional phagocytes with a very heavy daily load. However, unlike other professional phagocytes, the RPE cells are not replaced, so that any inefficiency in the degradation of phagosomes can build up over the life of the organism. It has been proposed that such inefficiencies might lead to pathogenesis and age-related visual impairment (Feeney, 1973; Sparrow and Boulton, 2005).

RPE cells are polarized epithelial cells, and the maturation of disk membrane phagosomes involves movement from the site of phagocytosis at the apical surface into the cell. In studies on mice lacking myosin-7a, it was shown that phagosome progression out of the actin-rich apical region was retarded (Gibbs et al., 2003). Myosin-7a has been demonstrated to be a functional actin motor (Udovichenko et al., 2002), and in humans, it is encoded by the gene that is defective in Usher syndrome 1B, a deaf-blindness disorder (Weil et al., 1995). Studies on the phagocytosis of latex beads by macrophages showed that the delivery of phagosomes to lysosomes appeared to entail dynamic

*M. Jiang and J. Esteve-Rudd contributed equally to this paper.

Correspondence to David S. Williams: dswilliams@ucla.edu

T. Diemer's present address is Dept. of Psychiatry, School of Medicine, University of California, San Diego, La Jolla, CA 92093.

C. Lillo's present address is Instituto de Neurociencias de Castilla y León, Salamanca 37007, Spain.

Abbreviations used in this paper: AMD, age-related macular degeneration; CTSD, cathepsin D; KHC, kinesin-1 heavy chain; KLC1, kinesin-1 light chain 1; MDA, malondialdehyde; MYO7A, heavy chain of myosin-7a; ONL, outer nuclear layer; OTAP, osmium, tannic acid, paraphenylenediamine; P, postnatal day; POS, photoreceptor outer segment; RPE, retinal pigment epithelium; STED, stimulated emission depletion; WT, wild type.

The Rockefeller University Press $30.00
J. Cell Biol. Vol. 210 No. 4 595–611
www.jcb.org/cgi/doi/10.1083/jcb.201410112

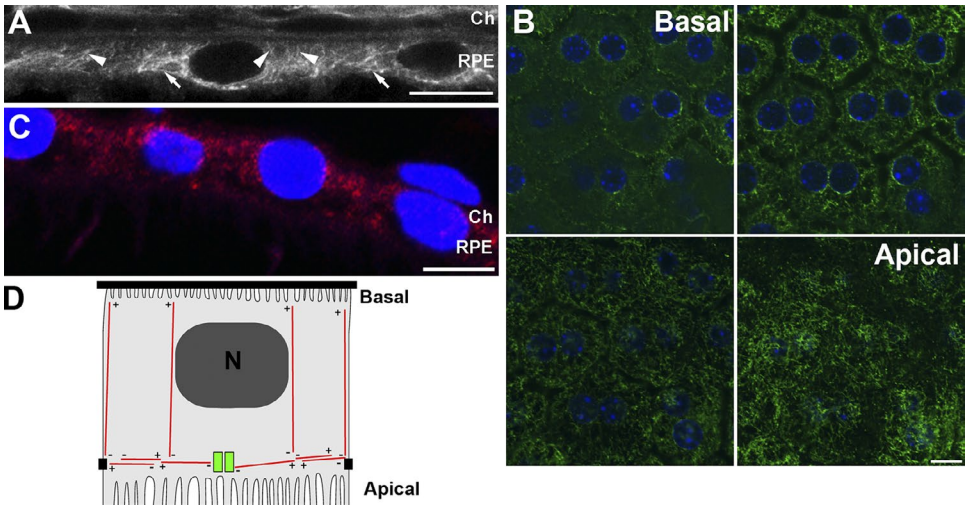

Figure 1. **Organization of microtubules in mouse RPE cells.** (A) STED super-resolution microscopy image of a section of the RPE from an albino mouse, labeled with α-tubulin antibodies. Arrowheads indicate vertical microtubules. Horizontal microtubules are evident, predominantly near the apical margin of the cell body (arrows). (B) Single-plane confocal microscopy images of RPE cells in whole-mount preparations, showing the organization of the microtubules (immunolabeled with anti–α-tubulin; green) at different apical-basal locations. (C) EB1 immunolocalization (red) in a section of an albino mouse RPE, indicating localization of the plus ends of the microtubules mainly in the basal region. Ch, choroid. (D) Diagram of the indicated organization and polarity of microtubules in RPE cells. Bars, 10 µm.

roles for molecular motors. Microtubules and associated motors were found to be required for transport of the beads from the cell periphery to the central region (Blocker et al., 1996, 1997, 1998). The unconventional myosin, myosin-5, was also found to be involved in regulating the movement of the phagocytosed beads from the periphery (Al-Haddad et al., 2001). In *Tetrahymena thermophilia*, a myosin, Myo-1, is required for the directed motility of latex-bead phagosomes (Hosein et al., 2005).

To study the motility and degradation of phagosomes from POS disk membranes, we have developed a primary RPE cell culture system in which the rate of phagosome degradation compares to that in vivo. We have complemented this approach with analyses in vivo, where POS disk phagocytosis is triggered according to a daily cycle at the beginning of the light phase (LaVail, 1976). Thus, phagocytosis of POS disks by the RPE represents a well-regulated system for the study of phagocytosis, as well as being a potentially important process for retinal health underlying vision.

With these approaches, we have analyzed the motility of POS phagosomes, and the importance of phagosome movement on phagosome degradation. Further, we have examined the long-term consequences of defective microtubule motor activity in the RPE, and thus demonstrate the impact of this activity on the development of an array of phenotypes found in age-related macular degeneration (AMD), a major cause of blindness in older humans.

Results

Microtubule organization in RPE cells

To determine the microtubule organization in mouse RPE cells, we imaged retinal sections as well as flat mounts of the posterior half of the eye, with or without the neural retina, using confocal and stimulated emission depletion (STED) super-resolution microscopy. Immunolabeling with α-tubulin antibodies showed microtubules throughout the cell body region. Vertically oriented microtubules extend across this region, from the level of the junctional complexes to near the basal surface (Fig. 1, A and B; and Fig. S1, A and B). An enrichment of EB1 labeling, which is concentrated at the plus ends of microtubules, was detected in the more basal region (Fig. 1 C), indicating that the majority of these apical-basal microtubules were oriented with their plus ends more basal. EM of RPE in which the microtubules were decorated with tubulin hooks to indicate polarity (Euteneuer and McIntosh, 1980) indicated a similar result: in 20 separate images from the basal half of the cell body, 92 out of 129 microtubules were decorated with hooks that indicated basal projection of their plus ends.

In addition to the vertical microtubules, we observed a meshwork of lateral microtubules in the apical part of the microtubule domain (Fig. 1, A, B, and D; and Fig. S1, C and D). These microtubules appear to be responsible for much of the nonbasal EB1 labeling, which appeared greater near the lateral plasma membrane (Fig. 1 C). In the center of the cell, many of the lateral microtubules appeared to emerge from the centrosome, but, closer to the plasma membrane, they were not associated with it (Fig. S1 D). Labeling by PARD3 or centrin antibodies indicated centrosomes in the apical part of the microtubule domain of some cells (Fig. S1, C and D). PARD3 labeling has been used as a marker for basal bodies (Fan et al., 2004; Atwood et al., 2013), and a primary cilium could be observed projecting into the actin domain of each cell (Fig. S1 C). Retinal sections and z-stacks of flat mounts showed that the lateral microtubules and the apical tips of the vertical microtubules juxtapose the basal limit of the apical network of actin filaments, which includes the actin ring associated with the junctional complexes (Fig. S1, B and C).

In confluent cultures of primary mouse RPE cells, the microtubule organization was found to be comparable to that in vivo, with vertical and horizontal arrays of microtubules, with the latter in the apical part of the cell body (Fig. S1, E–J). PARD3 labeling of basal bodies, evident in the same plane as the horizontal microtubules (Fig. S1, E–G), was detected in 66% of the cells.

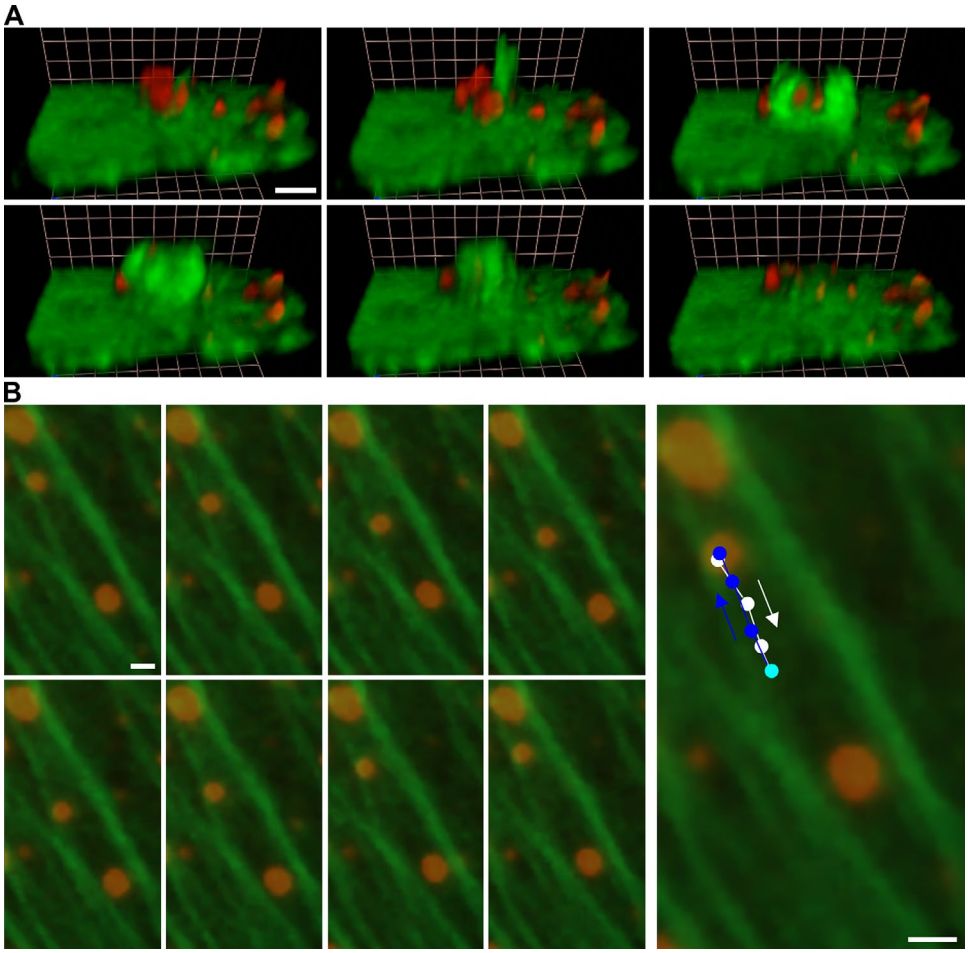

Figure 2. **Phagosome ingestion and transport.** (A) Time-lapse of 3D-reconstructed images, showing the ingestion of POSs (red) at the apical surface of an RPE cell expressing GFP (green). Each subsequent image represents a time lapse of 62 s (Video 1). (B) Time-lapse images of a primary mouse RPE cell in which microtubules are labeled with GFP–α-tubulin, and ingested POSs are labeled with Texas red. The track of one POS phagosome is shown in the enlarged image (right); different locations of the phagosome are indicated with white or blue spots, depending on the direction of the movement. Each subsequent image represents a time lapse of 2 s (Video 2). Bars: (A) 5 µm; (B) 2 µm.

In subsequent studies presented below, where we have quantitatively compared different regions of the RPE, the apical region is defined as the actin-rich domain, extending from the apical microvilli to the level of the junctional complexes. In some cases, the cell body was divided into the central and basal regions of the RPE, in which case the central region therefore contained the lateral microtubules.

Although significantly more difficult to generate, in the subsequent studies, primary cultures (Diemer et al., 2008) were preferred over cultures of RPE cell lines, which have been reported to lack some RPE polarity features (Lehmann et al., 2014), have reduced expression of a large proportion of "RPE signature genes" (Strunnikova et al., 2010), and typically exhibit kinetics of phagosome degradation that is much slower than that found in vivo and in primary RPE cultures (Finnemann et al., 2002; Mazzoni et al., 2014).

POS phagosomes move along microtubules in RPE cells

When primary mouse RPE cells are incubated with purified POSs, the POSs bind to the apical surface of the RPE cells, and then become ingested by phagocytosis, as illustrated by the accompanying time-lapse video (Fig. 2 A and Video 1). The ingested POS phagosomes then migrate from the apical region into the cell and are degraded (Gibbs et al., 2003), mimicking events that occur in vivo (LaVail, 1976; Herman and Steinberg, 1982).

To begin our investigation of this phagosome migration, we tested whether POS phagosomes could be observed moving along microtubules in live primary RPE cells. Microtubules were labeled with either GFP–α-tubulin or overexpressing EB3-GFP, and Texas red-X–labeled POSs were imaged after their ingestion by the cells. Motility along the labeled microtubules was evident as bidirectional movements, indicating the involvement of both plus and minus end–directed motors. The movements were punctuated with pauses, so that the overall movement was saltatory (Fig. 2 B and Video 2).

Association of MYO7A and KLC1 with POS phagosomes in RPE cells

To test for the association of motor proteins with POS phagosomes, cultured RPE cells were labeled with antibodies against rod opsin (RHO) to identify phagosomes, and against subunits of different motor proteins. MYO7A, the heavy chain of kinesin-1, and KLC1, a light chain of kinesin-1 (tetrameric conventional kinesin, containing two motor subunits and

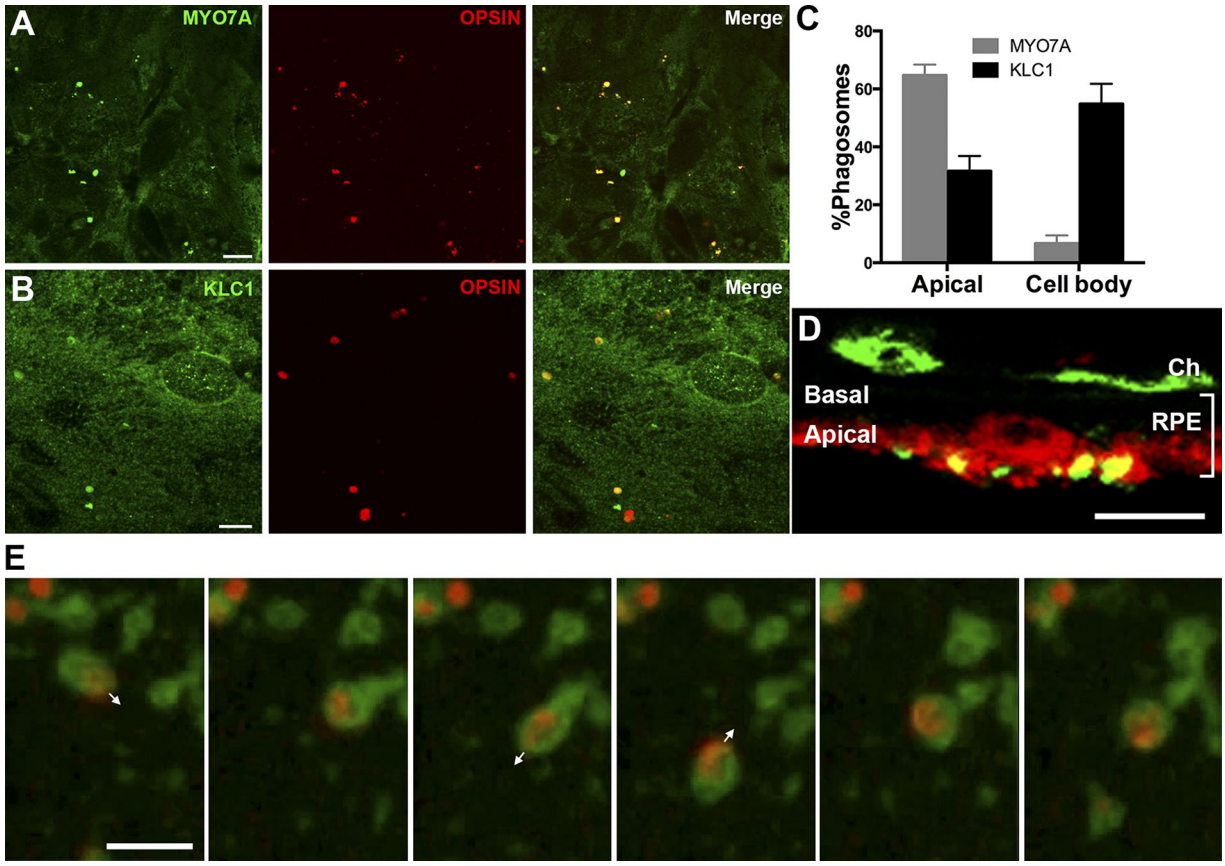

Figure 3. **Association of MYO7A and KLC1 with phagosomes.** (A and B) Mouse primary RPE cells were fed with mouse POSs and immunolabeled with a RHO mAb (mAb1D4 in A, mAb4D2 in B; red) and a MYO7A (A) or KLC1 (B) pAb (green). (C) Proportion of POS phagosomes associated with MYO7A and KLC1 antibody labeling in different regions of cultured RPE cells. The data illustrated in the graph were from albino RPE, and the phagosomes were identified by a mixture of RHO mAb1D4 and mAb4D2. Phalloidin-TRITC was used to identify the apical region. Error bars are ± SEM; n = 10 (KLC1) or 11 (MYO7A). (D) Immunofluorescence of an RPE section from an albino mouse, double labeled with MYO7A pAb (red) and RHO mAb1D4 (green). Bracket indicates the depth of the RPE. The neural retina was detached from the RPE; the green label at the apical RPE may represent phagosomes or tips of POSs that might have remained adhered to the RPE apical surface. The green label in the choroid (Ch) represents labeling of endogenous IgG by the secondary antibody. (E) Time-lapse fluorescence microscopy of a Texas red–labeled phagosome that has KLC1-YFP associated with it. Arrows indicate direction of movement. Each frame contains red and green channel images, which were acquired sequentially, so that the red and green fluorescence appear less colocalized when the phagosome moves at a faster speed. KLC1-YFP also labels motile endosome-like organelles. Panels are from the first segment of Video 3. Bars: (A and B) 10 µm; (D) 5 µm; (E) 1 µm.

two light chains), were observed to colocalize with some of the POS phagosomes (Fig. 3, A and B). Antibodies against KIF3A or KAP3, components of heterotrimeric kinesin-2, did not label the phagosomes.

To test whether MYO7A and KLC1 bound preferentially to phagosomes in different regions of the RPE, we classified the phagosomes according to their apical-basal location. Fig. 3 C shows that phagosomes in the apical region (identified by phalloidin-TRITC labeling) were associated more with MYO7A than KLC1, whereas those in the cell body associated more with KLC1 than MYO7A. This result was obtained regardless of whether phagosomes were from prelabeled POSs or labeled with RHO antibodies, whether the cells were albino or pigmented, and whether the cells were single- or double-labeled with MYO7A and KLC1 antibodies.

Early phagosomes can be detected with the RHO mAb1D4; the epitope of this mAb is lost at a very early stage in phagosome maturation (Esteve-Rudd et al., 2014; Wavre-Shapton et al., 2014). Coimmunocolocalization studies with MYO7A and KLC1 antibodies and RHO mAb1D4, using cultured RPE, showed that MYO7A was associated with 87 ± 3% of mAb1D4-labeled phagosomes, whereas KLC1 was associated with only 12 ± 2% of mAb1D4-labeled phagosomes (n = 10 for each; ±SEM). Collectively, these findings indicate that MYO7A associates primarily with early phagosomes in the apical actin domain, and that once they are delivered to the cell body region, they associate with microtubule motors. In retinal sections from mouse eyes fixed at light onset, MYO7A was detected primarily in the apical RPE, where it colocalized with mAb1D4-labeled phagosomes (Fig. 3 D), consistent with the same process occurring in vivo.

Next, we examined live RPE cells that had been transfected with a plasmid encoding KLC1-YFP and fed POSs that were prelabeled with Texas red-X succinimidyl ester. The labeled KLC1 was observed to associate with a variety of organelles, including some of the POS phagosomes. It remained with motile phagosomes as they moved in one direction, paused, and even when a phagosome reversed direction (Fig. 3 E and Video 3). There was no evidence that the intensity of the fluorescence signal from the tagged KLC1 changed significantly when a phagosome paused or reversed direction (Fig. 3 E and Video 3), suggesting that a relatively stable population of KLC1 molecules might remain with the phagosome, even as velocity changes.

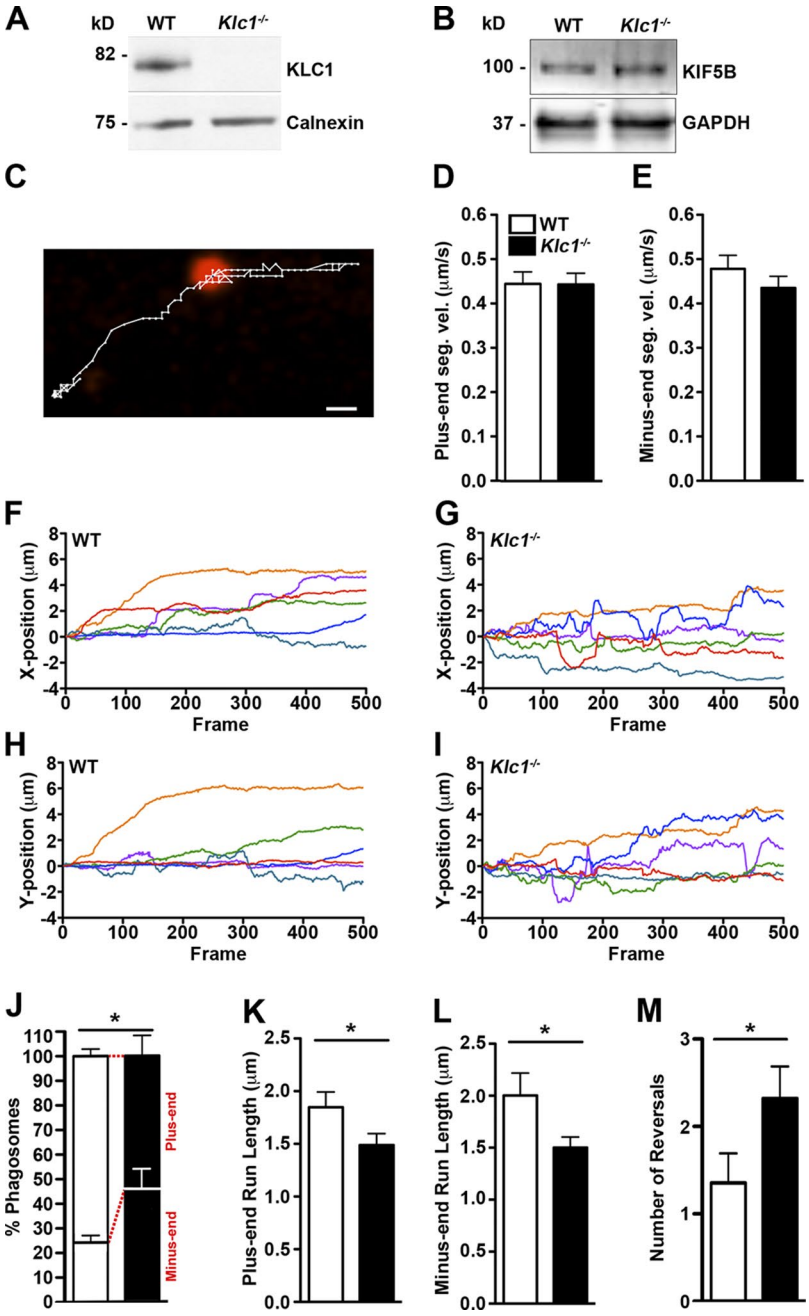

Figure 4. **Tracking of POS phagosomes in WT and *Klc1*$^{-/-}$ RPE cells.** (A and B) Western blots of WT or *Klc1*$^{-/-}$ eyecups, probed for KLC1 (A) or KIF5B (B), with calnexin (A) or GAPDH (B) as a loading control. (C) Example of a 3-min phagosome track (Video 4). Bar, 1 µm. (D and E) Mean segmental velocities of WT POS phagosomes in WT or *Klc1*$^{-/-}$ RPE, measured in plus and minus end directions. (D) n = 124 segments for WT and 121 segments for *Klc1*$^{-/-}$ (Mann–Whitney test, one-tailed, no significant difference). (E) n = 89 segments for WT and 101 segments for *Klc1*$^{-/-}$ (NSD). (F–I) Examples of tracks of POS phagosomes, with displacement in the x and y axes shown separately. (J) Proportion of POS phagosomes displaced toward the plus or minus end of the microtubules, at the end of a 3-min track, relative to their starting position. n = 3 separate experiments (paired t test, one-tailed; *, P = 0.03). (K and L) Mean run lengths, measured in plus and minus end directions. All run lengths ≥0.5 µm were included. (K) n = 90 runs each for WT and *Klc1*$^{-/-}$ (Mann–Whitney test, one-tailed; *, P = 0.02). (L) n = 69 runs for WT and 92 runs for *Klc1*$^{-/-}$ (*, P = 0.03). (M) Mean number reversals in direction per track. n = 34 tracks for WT and 47 tracks for *Klc1*$^{-/-}$ (*, P = 0.01). Error bars are means ± SEM.

Motility of POS phagosomes in *Klc1*$^{-/-}$ RPE cells

To determine the requirement of KLC1 function on the motility of POS phagosomes, we tracked motile POS phagosomes and measured parameters of their movements in primary RPE cultures from *Klc1*$^{-/-}$ mice and wild-type (WT) littermates. Western blot analysis confirmed that mouse eyecups from *Klc1*$^{-/-}$ mice lacked KLC1 (Fig. 4 A), and, consistent with studies on other tissues (Rahman et al., 1999; Reis et al., 2012), showed that levels of KIF5B, the major kinesin-1 heavy chain (KHC) expressed in RPE, were unaltered (Fig. 4 B). More specifically, quantitative immunoEM of retinal sections showed that KIF5B association with RPE phagosomes was not significantly different in *Klc1*$^{-/-}$ (2.7 ± 0.9 particles/µm of phagosome perimeter) compared with WT (3.2 ± 0.5 particles/µm).

Using spinning disk confocal microscopy of WT RPE cells (confirmed to be well-polarized) and acquisition of sequential z-axis stacks, we thus tracked early POS phagosomes in three dimensions. Tracks showed that the largest movements recorded were in the x and y axes (Fig. S2), indicating movement mainly along the microtubules oriented laterally. Because of this result, and to increase acquisition rate in the x and y axes, we acquired images in just one z-plane for further analysis of phagosome tracks in *Klc1*$^{-/-}$ RPE. Consistent with the fixed cells, observations of cells expressing EB1-EGFP showed that the majority of the lateral microtubules, especially in the center of the cell, were oriented with their plus ends directed away from the center. From regions that were used for phagosome tracking, we counted 89% of growing lateral microtubules (n = 130) oriented in this manner. Hence, microtubule plus or minus end–directed movements were based on whether they

moved away or toward the cell center, respectively. Fig. 4 C (Video 4) shows an example of a track; note how movements are interrupted by pauses in which the phagosome remains near one spot (also see Video 5).

The segmental velocities of POS phagosomes (defined as the mean velocity of each continuous run, which is a movement without pausing or changing direction by >135°) covered a range of velocities that extended beyond 1 µm/s. The mean segmental velocities in WT and *Klc1*$^{-/-}$ RPE were comparable in both plus and minus end directions (Fig. 4, D and E), indicating that the absence of KLC1 has no significant effect on velocity.

The tracks of POS phagosomes in WT and *Klc1*$^{-/-}$ RPE were nevertheless different (Fig. 4, F–I). In WT RPE, the net displacement of phagosomes during the 3-min tracks had a bias toward the plus end, but, in mutant RPE, there was no significant difference between the number of phagosomes that were displaced toward the microtubule plus ends or toward the minus ends from the starting point (Fig. 4 J). Measurements of the length of each run (i.e., "run length") showed that this distance was shorter in mutant RPE, both in the plus and minus end directions (Fig. 4, K and L). Consistent with these measurements, the frequency of reversals (a change in direction between 135 and 180°) was greater in the *Klc1*$^{-/-}$ RPE than in the WT (Fig. 4 M).

Basal migration of POS phagosomes in *Klc1*$^{-/-}$ RPE cells

These tracking measurements suggest that the regulation of POS phagosome motility on microtubules is impaired in *Klc1*$^{-/-}$ RPE cells. Although the measurements were made on movements along the lateral microtubules, we wondered whether this impairment might also be reflected in inhibited movement along the apical-basal axis. The loss of a plus end bias in net displacement might inhibit POS phagosome migration toward the basal surface if the same defect occurs on the apical-basal–oriented microtubules. Alternatively, the basal migration might be impeded by defects in lateral motility if loading on to the vertical microtubules is dependent on preceding lateral transport.

To test whether loss of KLC1 results in impaired basal migration of phagosomes, we determined the location of phagosomes in RPE cells, grown on filters, after the cells were fed POSs for 10 min and then fixed for confocal microscopy. The plotting of phagosome location along the apical-basal axis showed that, in *Klc1*$^{-/-}$ RPE, fewer phagosomes were located basally than in WT RPE (Fig. 5, A and B). Similarly, comparisons of retinal sections of *Klc1*$^{-/-}$ and WT mice, fixed 3 h after the onset of light, showed that more phagosomes were retained in the apical region of the mutant RPE (Fig. 5, C and D), thus providing in vivo evidence to support the cell culture observation.

Degradation of POS phagosomes in *Klc1*$^{-/-}$ RPE cells

In considering the motility of POS phagosomes and their degradation, we determined the distribution of cathepsin D (CTSD)–positive endosomes and lysosomes in the RPE. Immunolabeling of retinal sections showed that they were limited to the cell body (significant numbers were not detected in the apical domain) (Fig. 5, E–G), thus coinciding with the distribution of microtubules (Fig. 1). This observation suggests that phagosome motility along the lateral microtubules may be important for encounters with endosomes and lysosomes in the apical part of the cell body, and that the basal migration of phagosomes is

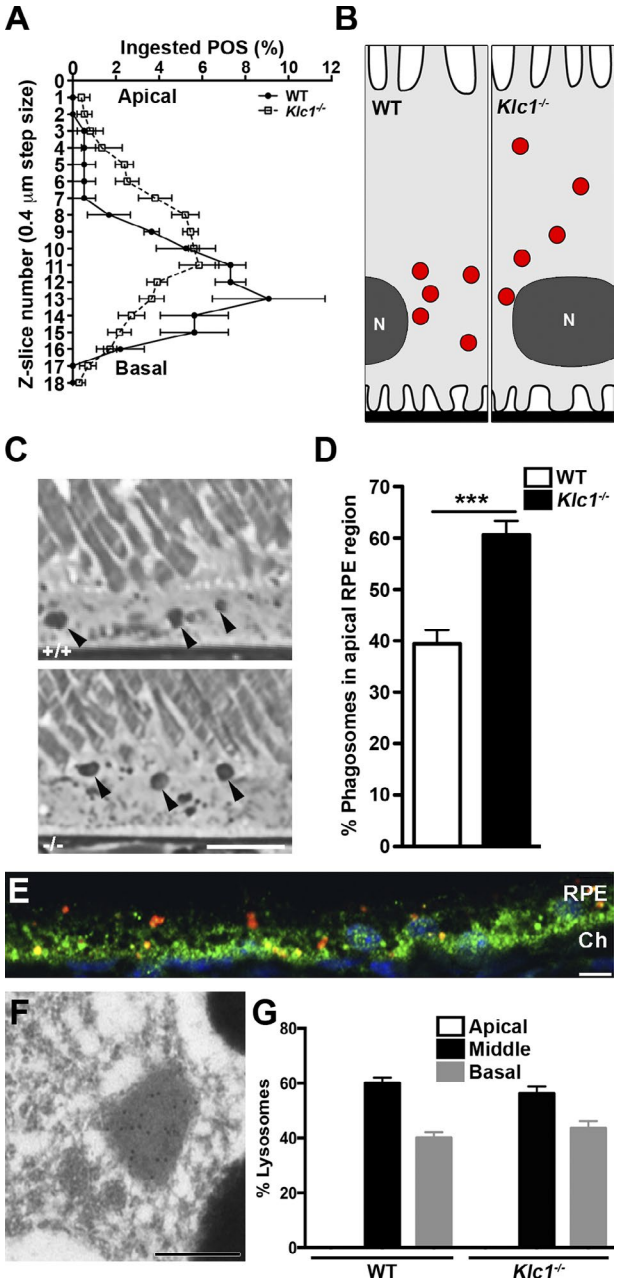

Figure 5. **Basal migration of POS phagosomes and lysosome localization.** (A) Apical-basal distribution of ingested POSs in primary cultures of WT or *Klc1*$^{-/-}$ RPE cells, after 10-min incubation with purified POSs. (B) Diagrammatic representation of results from A, showing that phagosomes in *Klc1*$^{-/-}$ RPE cells are located more apically than those in WT. (C) Semithin sections of albino retinas of WT (*+/+*) or *Klc1*$^{-/-}$ mice, within 0.5 mm of the optic nerve head. Images oriented as per orientation of the cultured RPE cells; distal tips of the POSs project down from the top. Arrowheads indicate phagosomes. (D) Proportion of phagosomes in the apical region of the RPE, in retinas fixed 3 h after light onset (***, P = 0.0002). (E) Vertical section of the RPE from albino mouse, with neuroretina detached, showing immunolabeling for CTSD (green) and RHO (red), plus DAPI labeling of nuclei (blue). The more apical (upper) POS phagosomes, which are newer, appear red, whereas the more basal phagosomes have mostly become phagolysosomes and appear yellow (merge of red and green). Ch, choroid. (F) EM showing a lysosome labeled with immunogold, representing CTSD localization. (G) Localization of CTSD-labeled endosomes and lysosomes in different regions of the RPE. Data are from immunoEM images of retinas fixed 3 h after light onset. Bars: (C and E) 10 µm; (F) 1 µm. Error bars are means ± SEM.

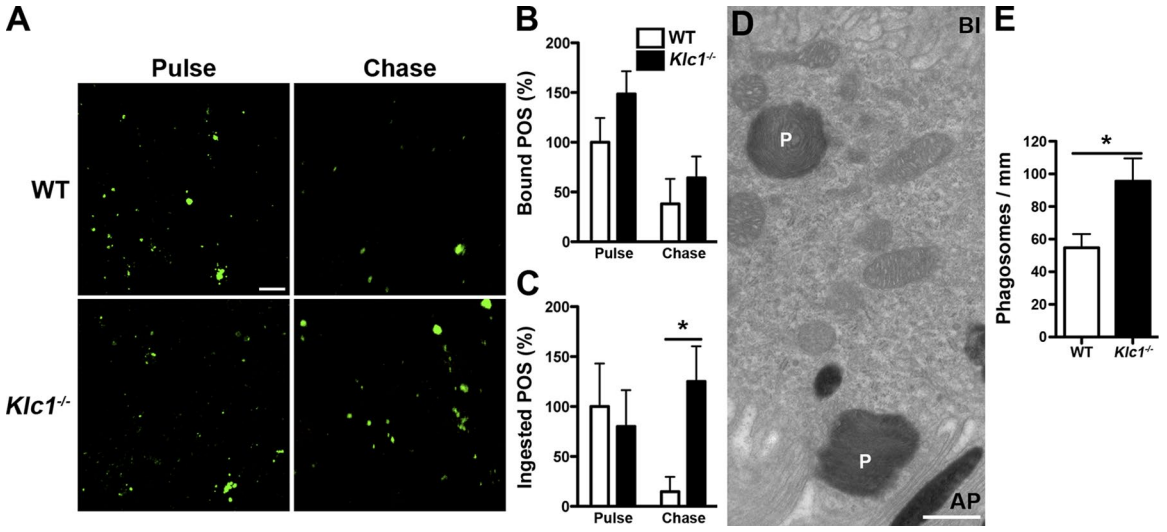

Figure 6. **POS phagosome degradation.** (A) RPE cells isolated from WT or *Klc1*$^{-/-}$ mice, showing bound and ingested WT POSs, labeled with RHO antibody, from a 15-min pulse/30-min chase experiment. (B and C) Bound (B) and ingested (C) POSs in WT and *Klc1*$^{-/-}$ RPE cells after a 15-min pulse/30-min chase. Data aggregated from four separate experiments; in each experiment, four to six fields of view from two to three Transwell filters were analyzed for each condition and each time point. The number of POSs is indicated as a percentage of the POS counted at the pulse time point in WT RPE. No significant difference was detected in the binding (B; Student's *t* test, two-tailed; P = 0.22) or ingestion (C; P = 0.69) of POS immediately after the pulse. However, after chase, although the number of bound POSs showed no significant difference between WT and *Klc1*$^{-/-}$ RPE cells (B; P = 0.45), there were many more ingested POS remaining in *Klc1*$^{-/-}$ than WT RPE (C; *, P = 0.01). (D) EM of *Klc1*$^{-/-}$ RPE. Phagosomes (P) were identified by the presence of disk membranes. AP, apical processes; BI, basal infoldings. (E) Number of phagosomes per length (millimeter) of RPE in WT or *Klc1*$^{-/-}$ mice 3 h after light onset (n = 5 animals per genotype; *, P = 0.009). Bars: (A) 10 µm; (D) 1 µm. Error bars are means ± SEM.

necessary for phagosomes to be exposed to the entire population of CTSD-positive endosomes and lysosomes.

Therefore, we next tested whether the degradation of POS phagosomes was impaired in *Klc1*$^{-/-}$ RPE cells. After incubating primary cultures of RPE cells with POSs, the POSs were removed, and then, after a "chase" period, remaining RHO-immunolabeled phagosomes were counted. A variety of "pulse-chase" times was tested. In all cases, the *Klc1*$^{-/-}$ cells contained more POSs after the chase period than the WT cells. The numbers of POSs bound to the apical surface, at any time, and the numbers of POSs ingested at the start of the "chase" period were both comparable in mutant and WT cells. Fig. 6 (A–C) shows images and data from a set of 15-min pulse/30-min chase experiments. The digestion rate of phagosomes in *Kif3a*$^{flox/flox}$ RPE cells that were treated with LV-*Cre* was not different from that in control cells (not depicted), indicating that heterotrimeric kinesin-2 was not required.

The rate of phagosome maturation was also studied in retinal sections from 2-mo-old mice maintained on a daily light–dark cycle. In our studies, the number of phagosomes in the mouse RPE peaks 30 min after light onset, and then declines over the following several hours (Gibbs et al., 2003). By EM, we found that, 3 h after the onset of light, there were nearly twice as many phagosomes in the RPE of *Klc1*$^{-/-}$ mice compared with the RPE of WT littermates. Phagosomes were counted per length of RPE, regardless of apical-basal location (Fig. 6, D and E); the depth of the RPE cell body was measured to be 6 µm in both WT and *Klc1*$^{-/-}$ retinas from 2-mth old mice.

Age-related pathology of *Klc1*$^{-/-}$ mouse retinas

Given the inhibition of phagosome degradation, both in cell culture and in vivo, we determined whether lack of KLC1 led to RPE pathogenesis in older animals. In this respect, we were limited to microscopy studies, as *Klc1*$^{-/-}$ mice, over 1 yr old, typically developed cataracts, consistent with the reported linkage of age-related cataracts to *KLC1* haplotypes in humans (Andersson et al., 2007; Zhang et al., 2013). The cataracts prevented us from successfully carrying out any rigorous fundus imaging, optical coherence tomography analysis, or electroretinogram studies.

By light and EM, differences in the health of *Klc1*$^{-/-}$ retinas, compared with the retinas of heterozygous or WT littermates, were evident in 18-mo-old mice, according to several parameters. A relative loss of photoreceptor cells was measured, mainly in the central dorsal retina (Fig. 7, A–C). To test for the accumulation of lipofuscin in the RPE, we first measured autofluorescence that was emitted from the RPE in retinal sections upon 488-nm excitation. This autofluorescence was found to be higher in *Klc1*$^{-/-}$ mice (Fig. 7, D and E; 545.2 ± 15 arbitrary units in WT vs. 778.9 ± 57.05 in *Klc1*$^{-/-}$ mice; P = 0.003). Next, we used EM to determine the extent of lipofuscin granule accumulation by measuring the area occupied by granules relative to the total cytoplasmic RPE area in apical-basal sections. There was significantly more accumulation by this measure in the RPE of *Klc1*$^{-/-}$ mice (5.5 ± 0.3% in controls vs. 7.1 ± 0.5% in *Klc1*$^{-/-}$ mice; P = 0.003).

EM also showed that Bruch's membrane (the basement membrane of the RPE) was thicker in the *Klc1*$^{-/-}$ retina. This thickening was found to be caused by basal laminar deposits (Fig. 7, F–I) and consequential expansion of the inner collagen layer of Bruch's membrane, which includes fibronectin (Fig. 7, J and K). Immunolabeling with antibodies against elastin and collagen IV, which are present in the elastin layer and choroidal basement membrane of Bruch's membrane, respectively (Marshall et al., 1992), showed no significant difference between

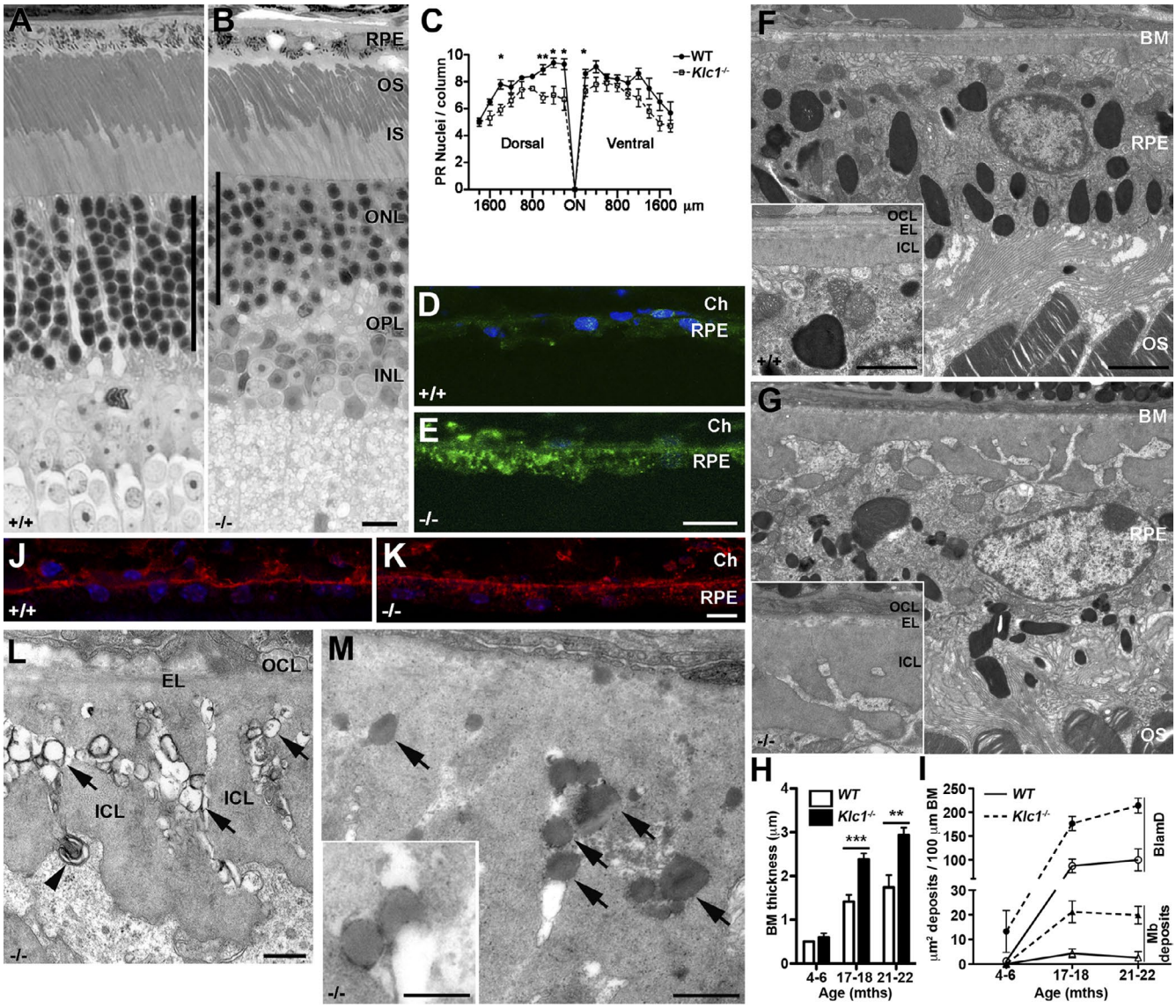

Figure 7. **Pathology in retinas of 18–20-mo-old *Klc1*$^{-/-}$ mice.** (A and B) Semithin sections of WT (A) and *Klc1*$^{-/-}$ (B) central retinas. The ONL (black bar) is thinner in the mutant. (C) Number (mean ± SEM) of aligned photoreceptor nuclei across the ONL (i.e., per column) in WT (n = 5; closed circles) and *Klc1*$^{-/-}$ (n = 6; open squares) mice. Note the significant loss of nuclei in the central retina of mutant mice (Student's t test; *, P < 0.05; **, P < 0.01). (D and E) Retinal sections showing autofluorescence (488-nm excitation, 500–600-nm emission) of RPE in WT (D) and *Klc1*$^{-/-}$ (E) mice. (F and G) EMs of RPE of control (F) and *Klc1*$^{-/-}$ (G) retinas showing that Bruch's membrane (BM) is thicker in the mutant than in the control. (H) Quantification of Bruch's membrane thickness in retinas of 4–6 (n = 4 WT and 4 *Klc1*$^{-/-}$; P = 0.33)-, 17–18 (n = 7 WT and 7 *Klc1*$^{-/-}$; ***, P = 0.0005)-, and 21–22 (n = 4 WT and 7 *Klc1*$^{-/-}$; **, P = 0.003)-month old animals. (I) Quantification of the sub-RPE basal laminar deposits (BlamD) and membranous (Mb) debris in retinas of 4–6 (P = 0.21 for BlamD), 17–18 (**, P = 0.001 for BlamD; **, P = 0.004 for Mb debris) and 21–22 (**, P = 0.002 for BlamD; *, P = 0.008 for Mb debris) months old WT and *Klc1*$^{-/-}$ animals. (J and K) WT (J) and *Klc1*$^{-/-}$ (K) retinas immunolabeled for fibronectin, showing that the enlargement of BM is mainly caused by an expansion of the inner collagen layer (which contains fibronectin). (L) EM of *Klc1*$^{-/-}$ RPE, showing electron-dense web-like material (arrowhead) and individual profiles in a sub-RPE aggregate of membranous vesicles (arrows) in the inner collagen layer of the BM (similar to the deposits shown in Fig. 3 of Curcio et al., 2005). (M) EM section of the aggregates, fixed by the OTAP method, which preserves neutral lipids. Solid particles are evident among the BlamD, rather than membrane vesicles with aqueous interiors. (Inset) A membrane surrounding the neutral lipids is evident. BM, Bruch's membrane; RPE, retinal pigment epithelium; OS, outer segments; IS, inner segments; ONL, outer nuclear layer; OPL, outer plexiform layer; INL, inner nuclear layer; OCL, outer collagen layer; EL, elastic layer; ICL, inner collagen layer. Bars: (A, B, D, E, J, and K) 10 µm; (F and G) 2 µm; (F and G insets) 1 µm; (L) 300 nm; (M) 500 nm; (M inset) 250 nM. Error bars are means ± SEM.

mutant and control, suggesting that these regions of Bruch's membrane were relatively unaffected. Within the expanded inner collagen layer, vacuoles and membranous debris were evident in conventionally fixed tissue (arrows in Fig. 7 L), but when fixed to preserve neutral lipids (using osmium, tannic acid, paraphenylenediamine [OTAP] postfixation), structures that appeared like solid lipid particles were observed (Fig. 7 M), very similar to those observed in postmortem eyes from AMD patients, using the same method of postfixation (Curcio et al., 2005). In some retinas, more extensive pathology was observed in the form of RPE cells congested with undigested whorls of membranes (Fig. S3 A). Moreover, in more deteriorated regions of retinas of 20–22-mo-old *Klc1*$^{-/-}$ mice, occasional examples of drusen-like structures and neovascularization were evident (Fig. S3, B–D). Comparable pathological changes were observed among mice on different genetic backgrounds (Fig. S3, E and F), including

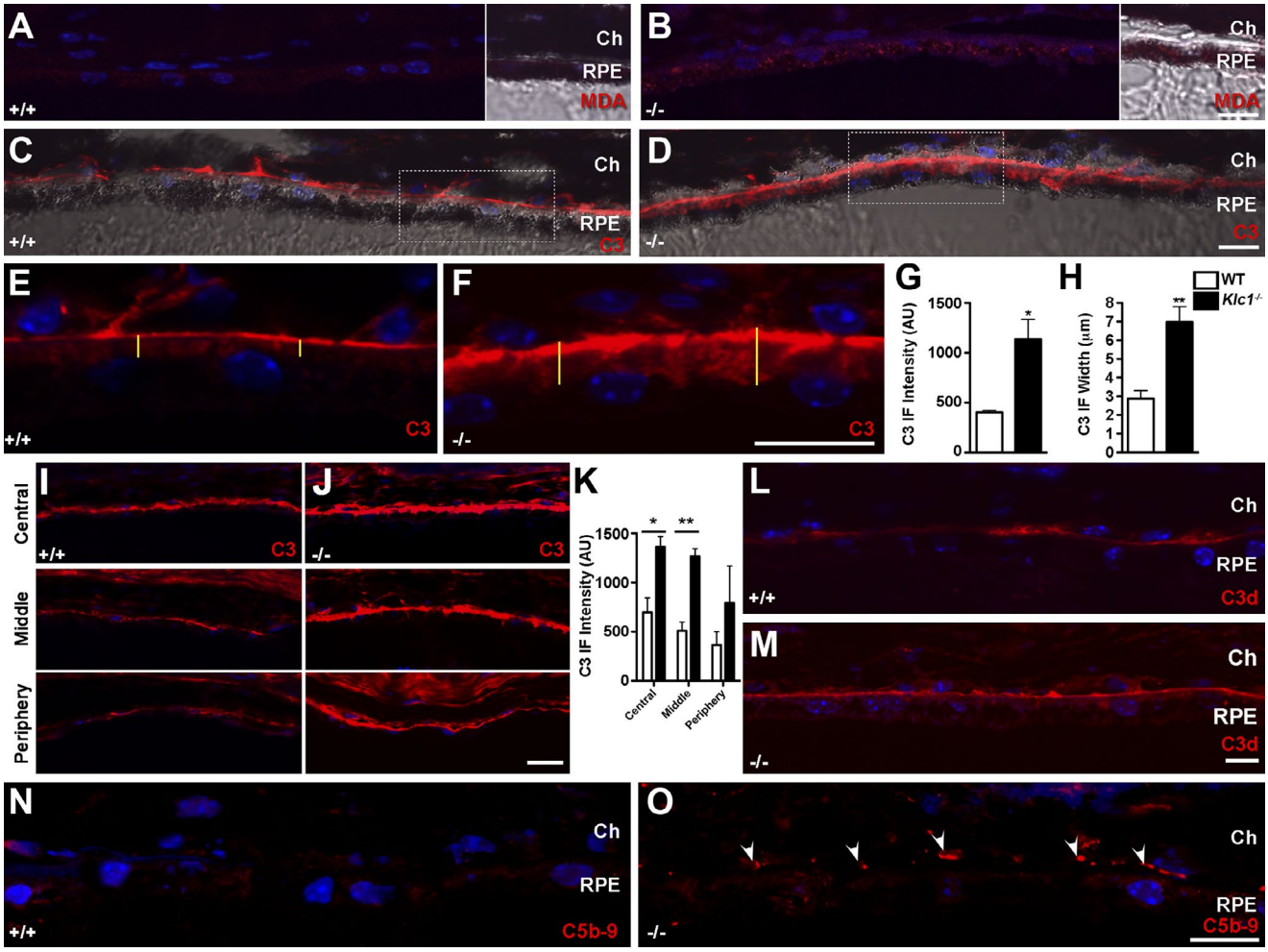

Figure 8. **Oxidative stress and complement activation associated with the RPE of 18–20-mo-old *Klc1*$^{-/-}$ mice.** (A and B) MDA immunoreactivity in WT (A) and *Klc1*$^{-/-}$ (B) retinal sections. Transmitted light images are on the right of each panel. (C and D) C3 immunoreactivity in WT (C) and *Klc1*$^{-/-}$ (D) retinal sections. (E and F) Amplified areas of C and D, respectively. Note the increase in the width of C3 immunoreactivity in the mutant (F), invading most of the cytoplasm of RPE cells. (G and H) Quantification of C3 immunofluorescence in terms of fluorescence intensity (G; *, P = 0.02) and width of the band of fluorescence (H; **, P = 0.005). At least five images, spanning the central/midcentral retina from at least three animals of each group, were analyzed. Student's *t* test (*, P < 0.05; **, P < 0.01). (I and J) C3 immunoreactivity in the central, middle, and peripheral retina of WT (I) and *Klc1*$^{-/-}$ (J) mice. (K) Quantification of C3 immunofluorescence in the central (*, P = 0.02), middle (**, P = 0.002), and peripheral (NS, P = 0.4) retina of WT and *Klc1*$^{-/-}$ mice; *n* = 3 animals. (L and M) Retinal sections of WT (L) and *Klc1*$^{-/-}$ (M) mice immunolabeled with antibodies against C3d. Note the higher immunolabeling in BM and the basal side of RPE cells in the mutant retina. (N and O) Retinal sections of WT (N) and *Klc1*$^{-/-}$ (O) mice immunolabeled for the C5b-9 complex, showing deposition of the membrane attack complex in some areas of the innermost side of the choroid, adjacent to the RPE, in *Klc1*$^{-/-}$ mice. Ch, choroid; RPE, retinal pigment epithelium. Bars, 10 µm. Error bars are means ± SEM.

inbred and outbred mice that were demonstrated by genotyping to lack the *Crb1*$^{rd8/rd8}$ mutation; this mutation is present in some C57BL/6 lines (Mattapallil et al., 2012; Luhmann et al., 2015).

Complement activation and oxidative stress in old *Klc1*$^{-/-}$ mouse retinas

Oxidative stress and hyperactivation of the complement pathway have been implicated in the pathogenesis of AMD. We tested for the presence of these characteristics in 18-mo-old *Klc1*$^{-/-}$ mouse retinas. Levels of malondialdehyde (MDA)-adducted proteins were labeled in retinal sections with an MDA antibody, as an indicator of oxidative stress. An increase in MDA immunoreactivity was observed in the RPE of *Klc1*$^{-/-}$ mice (Fig. 8, A and B).

To assess activation of the alternative pathway of the complement system, immunolabeling with an antibody that recognized the complement component, C3, and its activation products C3b, iC3b, C3d, and C3dg was performed. C3 immunolabeling was significantly more intense in the RPE of *Klc1*$^{-/-}$ mice (Fig. 8, C–H). In aged WT mice, the immunolabeling was restricted to the walls of choroidal blood vessels, Bruch's membrane and, to a lesser extent, the basal membrane of RPE cells. However, in *Klc1*$^{-/-}$ retinas, C3 immunolabeling was more intense at Bruch's membrane and on the basal side of the RPE. The increase in immunoreactivity was higher in the central retina than in the periphery (Fig. 8, I–K). No difference was observed in the immunolabeling of C3a or C3b/iC3b, which are elevated under acute inflammatory conditions, suggesting that the observed increase in C3 labeling could correspond to a more chronic inflammatory situation. Increased immunolabeling of Bruch's membrane and the basal RPE in *Klc1*$^{-/-}$ retinas with antibodies against C3d, a marker for chronic complement activation, supports this notion (Fig. 8, L and M). Lastly, we tested for the presence of the membrane attack complex, which is the

final step of complement system terminal pathway, using antibodies against the complement components, C5b-9. Immunoreactivity for the membrane attack complex was observed in some areas of the RPE–choroid complex from *Klc1*$^{-/-}$ mice, whereas none was detected in age-matched WT mice (Fig. 8, N and O).

Discussion

By live-cell imaging, we have shown that POS phagosomes move bidirectionally along microtubules in RPE cells. KLC1 associates with the phagosomes. In the absence of KLC1, the speed of the phagosome movement appears to be unaltered, but the regulation of the movement is impaired. The phagosomes migrate less efficiently through the RPE cell body and are degraded more slowly. Characteristics of AMD pathogenesis appear in the retinas of old *Klc1*$^{-/-}$ mice.

Myosin-7a and microtubule motor transport in relation to POS phagosome maturation

The microtubule organization in the mouse RPE differed somewhat from that reported for β- and γ-tubulin labeling of chicken RPE, where it was suggested that the microtubules are directed basally and laterally from an apical centrosome (Rizzolo and Joshi, 1993). Here, we observed some lateral microtubules emerging from an apical centrosome, but other lateral microtubules in the periphery of the cell, as well as the vertical microtubules, were not associated with a centrosome. In this respect, the microtubule organization observed here compares more closely to that reported for other confluent epithelial cells (Bacallao et al., 1989; Gilbert et al., 1991). It has been reported that rat RPE cells lose their cilia during the first postnatal weeks (Nishiyama et al., 2002). Our detection of RPE primary cilia in whole mounts of retinas from postnatal day 30(P30) mice indicates otherwise, consistent with a recent study that suggests loss of cilia in adult RPE is an artifact that is introduced if the neural retina is removed from the RPE (Lehmann et al., 2014).

POS phagosome maturation coincides with a migration from the apical surface of the cell and then through the cell body (Herman and Steinberg, 1982; Gibbs et al., 2003; Esteve-Rudd et al., 2014; Wavre-Shapton et al., 2014). An indicator of an early stage of POS phagosome maturation is the loss of the RHO C-terminal epitope, recognized by mAb 1D4. POS phagosomes labeled by this mAb are present in the apical RPE (Esteve-Rudd et al., 2014; Wavre-Shapton et al., 2014). Taking both RHO immunolabeling and subcellular location as indicators of POS phagosome maturity, our results show that MYO7A is associated with early phagosomes, whereas KLC1 is associated more with later-stage phagosomes.

The movement of latex-bead phagosomes to microtubule motors appeared to be inhibited by association with myosin-5a in macrophages (Al-Haddad et al., 2001). Myosin-5a and myosin-7a have comparable roles in the motility of melanosomes; both capture melanosomes from microtubule transport: myosin-5a in melanocytes (Wu et al., 1998) and myosin-7a in RPE cells (Gibbs et al., 2004; Lopes et al., 2007). However, myosin-7a appears to facilitate rather than inhibit the delivery of POS phagosomes to the microtubules in the RPE. Lack of MYO7A was found to delay the migration of POS phagosomes out of the apical region of the RPE (Gibbs et al., 2003). Therefore, in the RPE, the delivery of POS phagosomes appears to involve a cooperative relay, with myosin-7a transport of early phagosomes through the apical actin filament network, followed by microtubule motor transport of more mature phagosomes in the cell body, where the CTSD-containing endosomes and lysosomes are located.

Microtubule motor transport of POS phagosomes

Our results indicate that, once on the microtubules, the POS phagosomes are transported by conventional kinesin, kinesin-1. Heterotrimeric kinesin-2, which has been shown to be a plus-end motor for organelles, such as melanosomes, in other cells (Tuma et al., 1998), was not detected on POS phagosomes, and loss of its function, unlike lack of KLC1, had no effect on the rate of phagosome degradation. To achieve the bidirectional movements, kinesin-1 is presumably paired with dynein. Bidirectional movements have been reported for a variety of organelles and vesicles (Welte, 2004), including even those that move persistently in one direction, such as mitochondria (Saxton and Hollenbeck, 2012), autophagosomes (Maday et al., 2012), and vesicles (Encalada et al., 2011), as they undergo axonal transport. Different models have been proposed to explain how kinesin-1 and dynein might be regulated to generate bidirectional transport (Fu and Holzbaur, 2014). In one model, direction of travel is the outcome of a tug of war between the opposing motors associated with the cargo. A change in direction is effected by a change in the relative number of engaged kinesin-1 and dynein molecules (Welte, 2004; Müller et al., 2008). Support for this model includes studies of neuronal vesicles (Hendricks et al., 2010) and endosomes (Soppina et al., 2009). Recently, however, studies have shown cargoes that maintain a stable population of associated motors when changing direction, or even pausing, suggesting regulation of motor activity rather than relative changes in motor association (Encalada et al., 2011). From our observations of the association of fluorescently tagged KLC1 with POS phagosomes in live cells, it appeared from the fluorescence signal that the amount of KLC1 associated with a phagosome did not change appreciably as the organelle changed direction or paused, which is more consistent with a stable motor population whose activities are regulated.

Requirement of KLC1 in POS phagosome motility

Kinesin light chains have been proposed to function in either cargo binding or modulation of motor activity (Pernigo et al., 2013; Fu and Holzbaur, 2014). KLC1 is predominant in neuronal tissues (Rahman et al., 1998). The lack of KLC1, although important with respect to POS phagosome degradation and long-term retinal health, had no detectable effect on the ability of the phagosomes to move along microtubules; segmental speed in *Klc1*$^{-/-}$ RPE was not significantly different from that in WT RPE. On the other hand, KLC1 was found to be important in regulating phagosome bidirectionality; our tracking data showed that mean run length was decreased and reversal frequency was increased in *Klc1*$^{-/-}$ RPE cells. Interestingly, run length was shorter in both plus and minus end directions. These findings point to a regulatory function for KLC1, rather than essential linkage of POS phagosomes to kinesin transport.

KLC1 has been shown previously to promote autoinhibition of KHC (Verhey et al., 1998; Friedman and Vale, 1999). However, the present observations are more consistent with a

role in which KLC1 modulates the switching between kinesin-1 and dynein motor activity, and thus potentially a role that affects the whole motor complex, including dynein as well as KHC. Studies of the axonal transport of vesicles containing prion protein have shown that KLC1 is also required for normal retrograde transport activity (Encalada et al., 2011). Similar results have been found in a study of kinesin-1 transport of amyloid precursor protein along axons in *Drosophila*; in this study, it appeared that interactions between KLC and dynein intermediate chain are important in the switch between plus and minus end–directed movement (Reis et al., 2012).

In addition, an important coordinator of kinesin and dynein motors in the regulation of directionality is the motor-scaffolding protein, JIP1 (c-Jun N-terminal kinase–interacting protein 1), which binds KLC and KHC, as well as the dynein–dynactin complex (Verhey et al., 2001; Fu and Holzbaur, 2013). In the transport of autophagosomes along axons, LC3, on the surface of the autophagosomes, binds to JIP1 and thus influences directionality (Fu et al., 2014). Recent studies have shown that a portion of POS phagosomes becomes decorated by LC3 and converges on the autophagic pathway (Kim et al., 2013; Frost et al., 2014), suggesting the possibility of comparable regulation for some of the POS phagosomes.

Importance of POS phagosome motility for efficient degradation

Earlier studies on the phagocytosis of latex beads by macrophages concluded that the movement of the phagosomes along microtubules likely facilitates the interaction of phagosomes with endosomes and lysosomes (Rabinowitz et al., 1992; Desjardins et al., 1994). Our measurements of phagosome movements in *Klc1*$^{-/-}$ RPE cells point to two defects that could contribute to impaired phagosome degradation. First, the measured defects in early phagosome motility, such as shorter run lengths, along the lateral microtubules might reduce the probability of encountering an endosome or lysosome in the apical part of the cell body. Evidence for interactions between early POS phagosomes and endosomes in the RPE has been indicated from fixed tissue (Bosch et al., 1993; Wavre-Shapton et al., 2014). Second, the observed retardation of basal migration of phagosomes in *Klc1*$^{-/-}$ RPE would inhibit exposure to the entire population of CTSD-positive endosomes and lysosomes, which is distributed throughout the cell body (Fig. 5, E and G).

RPE pathogenesis from inefficient POS phagosome degradation

For decades, it has been proposed that inefficiencies in POS phagosome degradation promote an increased accumulation of lipofuscin and sub-RPE deposits, leading to RPE pathogenesis and age-related visual impairment, as in AMD (Hogan, 1972; Feeney, 1973; Feeney-Burns and Eldred, 1983; Sparrow and Boulton, 2005; Sparrow et al., 2012; Bowes Rickman et al., 2013). However, reports of experimental evidence that links defects in phagosome degradation with this RPE pathology have been limited to studies with mice expressing a mutant form of CTSD or the RAB escort protein, REP1. In the mutant *CTSD* transgenic mouse, sub-RPE deposits and photoreceptor degeneration were observed (Rakoczy et al., 2002), and in a conditional *Chm*$^{-/-}$ mouse, abnormally high accumulation of lipofuscin and sub-RPE deposits were also reported (Wavre-Shapton et al., 2013). CTSD is abundant in RPE lysosomes and is a major contributor to rhodopsin proteolysis (Regan et al., 1980), so that inhibited phagosome degradation appears to be the primary defect in the *CTSD* mouse. REP1 facilitates isoprenyl modifications of RAB GTPases and is encoded by the *CHM* gene, which is mutant in the retinal degeneration choroideremia (Seabra et al., 1993). Decreased expression of REP1 in the RPE has been shown to inhibit POS phagosome degradation (Krock et al., 2007; Gordiyenko et al., 2010). The mechanism by which this inhibition occurs is unclear, but it could be caused by the inability of underprenylated RAB proteins to link motor proteins to the phagosomes.

Interestingly, mutant *CHM* results in underprenylated RAB27A (Seabra et al., 1995), which is the RAB that links myosin-7a to melanosomes (Futter et al., 2004; Gibbs et al., 2004). However, although we have suggested here that myosin-7a functions in a cooperative relay with microtubule motors to transport POS phagosomes, myosin-7a appears to be involved in a less critical leg of the relay. A delay in the clearance of phagosomes from the actin-rich, apical RPE has been detected in *Myo7a* mutant RPE, but unlike that observed here with *Klc1*$^{-/-}$ mice, there was no delay in phagosome degradation detectable in vivo (Gibbs et al., 2003), and *Myo7a* mutant mice do not undergo detectable RPE pathogenesis (Williams, 2008).

Comparison with pathology of AMD

In this study, we found not only that the *Klc1*$^{-/-}$ mouse manifests slowed POS phagosome degradation, coupled with subsequent increased autofluorescence, lipofuscin granules, and basal laminar deposits, but we also observed the presence of other characteristic AMD phenotypes. First, we examined the membranous structures that accumulated within the basal laminar deposits. In a previous study on postmortem AMD retinas, similar structures were observed, but they were shown not to be an accumulation of membrane vesicles with aqueous interiors. Instead, they appear to arise from the deposition of neutral lipids, which, when preserved with the OTAP secondary fixative, appeared solid (Curcio et al., 2005), like the structures we observed in *Klc1*$^{-/-}$ RPE (Fig. 7 M), after using this preservation procedure (see Materials and methods). OTAP secondary fixation was originally used to preserve lipid droplets in atherosclerosis (Guyton and Klemp, 1988), with the paraphenylenediamine preserving osmium-treated neutral lipids, such as cholesterol and apolipoproteins. Therefore, it appears that excessive amounts of neutral lipids accumulate under the *Klc1*$^{-/-}$ RPE, and this characteristic is a major aspect of AMD (Pikuleva and Curcio, 2014).

Second, we found that the *Klc1*$^{-/-}$ RPE was associated with increased oxidative stress and activation of the complement pathway (Fig. 8), two other hallmarks of AMD (Anderson et al., 2010; Weismann et al., 2011). Oxidative stress adducts and components of the complement system have been found to accumulate in drusen and sub-RPE deposits of patients with AMD (Weismann et al., 2011; Shaw et al., 2012), and mice with mutations making them prone to oxidative stress or dysregulation of the complement pathway have been presented as models of AMD (Imamura et al., 2006; Justilien et al., 2007; Hollyfield et al., 2008; Ufret-Vincenty et al., 2010). In the *Klc1*$^{-/-}$ mice, however, the accumulation of oxidative stress adducts and complement activation seems more likely to be a downstream consequence of defective phagosome processing, rather than the primary event leading to AMD-like pathology. We did not observe any abnormal accumulation of oxidized material or complement proteins in younger *Klc1*$^{-/-}$ mice, even though sections

of their retinas showed that they exhibited abnormal phagosome localization and degradation.

Beyond oxidative stress and complement dysregulation, we also observed, in some *Klc1*$^{-/-}$ retinas, the presence of structures resembling drusen and the invasion of the RPE and photoreceptor layers by neovascularization (Fig. S3). The latter is characteristic of a late and severe stage in AMD, known as "wet" AMD. In humans, evidence of large drusen in fundus images is an indicator of early- and intermediate-stage AMD. It is important also to mention that the AMD lesions, known as basal linear deposits, which form internal to the inner collagenous layer of Bruch's membrane, were not detected in the *Klc1*$^{-/-}$ retina. This difference is to be expected, given that basal linear deposits form mostly in the fovea (Curcio et al., 2013), a small central region of the macula that contains only cone photoreceptors (Osterberg, 1935), which is not present in a mouse retina.

In summary, our findings on the age-related pathogenesis of the *Klc1*$^{-/-}$ mouse retina indicate many similarities with AMD in humans. Further, an important aspect of this study is the demonstration that the AMD-like phenotypes can be elicited upstream by defects in intracellular motility.

Materials and methods

Animals

All procedures conformed to institutional animal care and use authorizations. The *Klc1*$^{-/-}$ mutant mice (Rahman et al., 1999) and WT littermates originated from a colony that was on the C57BL/6J background, as used in a previous study (Stokin et al., 2005). In the *Klc1*$^{-/-}$ mutant mice, an exon that encoded a 72–amino acid sequence starting at QHSDSSA and ending at NILALVY was removed, resulting in out of frame translation of the remainder of the KLC1 gene (Rahman et al., 1999). Initial microscopy studies were performed on mice from this original colony. Later studies included mice from two separate colonies, both of which were derived from this original colony: one colony was the result of one or two backcrosses to C57BL/6NHsd (Harlan Laboratories, Inc.); and the other resulted from a cross with outbred HSD non-Swiss albino mice (Harlan Laboratories, Inc.), and subsequent breeding of the F1 generation (which provided more robust litters, with a greater proportion of surviving *Klc1*$^{-/-}$ pups, than the inbred colony). For RPE primary cell studies, pigmented animals were chosen to facilitate cell isolation. In all cases, mating was established as heterozygous × heterozygous pairs, thus yielding homozygous mutant and WT controls, as well as heterozygous littermates. Homozygous mutants were distinguished from the WT controls by genotyping, as described previously (Rahman et al., 1999). Mice were kept on a 12-h light/12-h dark cycle under 10–50-lux fluorescent light during the light cycle.

Cell culture

RPE primary cells were isolated from mouse retinas as described previously (Gibbs and Williams, 2003). In brief, intact eyes were removed from 9–15-d-old mice and washed twice in DMEM (high glucose). They were then incubated with 2% (wt/vol) dispase in DMEM (high glucose) for 45 min at 37°C. The eyes were washed twice in growth medium (GM) that consisted of DMEM (high glucose) plus 10% bovine FBS, 1% penicillin/streptomycin, 2.5 mM L-glutamax, and 1× MEM nonessential amino acids. All the reagents were from Invitrogen. After removal of the anterior cornea, lens, capsule, and iris-pigmented epithelium, the resulting posterior eyecups were incubated in GM for 20 min at 37°C. The neural retina was removed, and sheets of RPE were then peeled off from Bruch's membrane, washed, and then cultured. For live-cell imaging, cells were cultured on 24-well Transwell filter inserts (Corning) and imaged in a closed bath chamber (RC-43C; Warner Instruments) or cultured and imaged in 8-well coverglass chambers (LABTEK; Thermo Fisher Scientific) in complete GM. ARPE-19 cells (ATCC), from an immortalized human RPE cell line, were maintained in DMEM/F12 (Invitrogen), supplemented with 10% FCS (Invitrogen) and 1% penicillin-streptomycin liquid containing 10,000 U penicillin and 10 mg streptomycin in 0.85% saline (Invitrogen). For live-cell imaging, they were grown in glass-bottom Petri dishes (MatTek Corporation). All cells were maintained at 37°C with an atmosphere of 5% CO_2.

POS phagocytosis in cell culture

POS isolation. WT Mouse POSs were isolated using an OptiPrep (Sigma-Aldrich) step gradient in a method that was modified from Tsang et al. (1998). Mice were dark adapted overnight. Retinas were removed and placed in buffer A (130 mM NaCl, 3.6 mM KCl, 2.4 mM $MgCl_2$, 1.2 mM $CaCl_2$, 0.02 mM EDTA, and 10 mM Hepes, adjusted to pH 7.4 with KOH), with six to eight retinas/milliliter, on ice, under infrared illumination, and homogenized with 6–10 strokes using a 2-ml glass pestle. After brief centrifugation (100 *g*, 1 min), 0.75 ml supernatant was added to the top of each gradient that contained 0.75-ml steps of 8, 10, and 15% OptiPrep in buffer A in 4-ml centrifuge tubes. The tubes were centrifuged for 20 min at 12,000 *g* at 4°C in a swinging bucket rotor (HB-6; Sorvall) without braking. POSs were collected from the 10–15% interface, diluted threefold with buffer A, and centrifuged for 10 min at 10,000 *g* at 4°C. The pellet containing the POSs was resuspended with GM, and the concentration of intact POSs was determined with a hemocytometer under phase microscopy. POSs were used directly or labeled with Texas red-X, or Fluorescent red 646 reactive (Sigma-Aldrich), or Alexa Fluor 647 NHS ester (succinimidyl ester) according to the manufacturer's instructions. After incubation with the dyes for 1 h at 4°C, POSs were pelleted at 7,500 rpm for 5 min and washed extensively with buffer A. The final pellet was resuspended in RPE GM. For studies on ARPE19 cells, POSs were obtained from frozen bovine retinas that were thawed in buffer A, vortexed for 40 s, and processed as for mouse POSs, using OptiPrep step gradients.

POS degradation assay. Primary RPE cells on Transwell filters were incubated with 150 µl POS solution (10^7 POSs/ml) at 37°C and 5% CO_2. Cells were then washed extensively with PBS and either processed immediately for immunofluorescence analysis (pulse time point) or chased for appropriate periods of time, and then processed for immunofluorescence.

Bound and ingested POSs were identified and distinguished from each other, as described previously (Gibbs et al., 2003). In brief, cells were washed three times in PBS and blocked in blocking buffer (PBS plus 1% goat serum), and the bound (but not ingested) POSs were labeled with rabbit anti-RHO polyclonal antibody (pAb01; Liu et al., 1999), followed by an Alexa Fluor 568–nm-conjugated goat anti–rabbit antibody (Molecular Probes) for 1 h. Cells were then washed three times in PBS and permeabilized with 50% ethanol for 5 min at RT, and incubated with pAb01 again, followed by an Alexa Fluor 488–nm-conjugated secondary antibody (Molecular Probes) to label both bound and ingested POSs. The Transwell filters were excised and mounted with FLUORO-GEL (Electron Microscopy Sciences).

Immunofluorescence of phagosomes and motor proteins. RPE primary cells were isolated as described above and kept for 3 d in culture. Cells were fed POSs for 15 min and then fixed with buffered 4% formaldehyde for 15 min and then 50% ethanol for 5 min. After incubation with blocking solution (0.5% BSA in PBS, pH 7.4) for 45 min at RT, cells were incubated with primary antibodies for 1 h at RT in blocking buffer. To test for motor association in relation to location of phagosomes, two methods were used, using pigmented (from C57BL6

mice) or albino (from BalbC mice) cells. In one method, the POSs were prelabeled with the dye, Fluorescent red 646 reactive (Sigma-Aldrich), to permit phagosome identification, and the cells were double labeled with mouse anti-MYO7A mAb (clone 138-1; Developmental Studies Hybridoma Bank) and rabbit anti-KCL1 pAb (Santa Cruz Biotechnology, Inc.). In the other method, POS phagosomes were identified by immunolabeling, using a mixture of RHO mAb1D4 and 4D2, and the apical region of the RPE cells was identified by phalloidin-TRITC. Rabbit anti-MYO7A pAb2.2 (Liu et al., 1997) and rabbit anti-KCL1 pAb (Santa Cruz Biotechnology, Inc.) were used on separate filters of cells. To test for motor association of RHO mAb1D4-labeled phagosomes, cells were double labeled with the mAb1D4, together with the MYO7A pAb2.2 or the KCL1 pAb. After primary antibody incubation, cells were washed and incubated with Alexa Fluor–conjugated secondary antibodies for 45 min at RT and mounted with FLUORO-GEL (Electron Microscopy Sciences).

Western blot analysis

The RPE-choroid was isolated from WT and *Klc1*$^{-/-}$ mouse eyes and lysed in 20 mM Tris, pH 7.4, 5 mM $MgCl_2$, 10 mM NaCl, 1 mM DTT, and 1× protease inhibitors (Sigma-Aldrich). Equivalent amounts of sample were run on a 4–12% NuPAGE Bis-Tris gel (Invitrogen). After transfer, membranes were blocked with Odyssey blocking buffer (LI-COR; Lincoln) and probed with rabbit anti-calnexin (Enzo Life Sciences), rabbit anti-KIF5B (Abcam), rabbit anti-KLC1 (Santa Cruz Biotechnology, Inc.), and mouse anti-GAPDH (EMD Millipore). Goat anti–mouse IRDye 680, donkey anti–rabbit 680, or donkey anti–rabbit 800 secondary antibody (LI-COR; Lincoln) was used. Membranes were imaged with the Odyssey infrared imaging system (LI-COR; Lincoln).

Imaging of phagosome motility

RPE primary cultures from WT and *Klc1*$^{-/-}$ animals were incubated with POSs that had been labeled with Texas red-X or Fluorescent red 646 reactive (Sigma-Aldrich), or Alexa Fluor 647 NHS ester, a succinimidyl esterthat reacts almost exclusively with amines (Life Technologies). Phagosomes were then imaged using a spinning disk confocal microscope system (UltraVIEW ERS; PerkinElmer) containing a microscope (Axio Observer.A1; Carl Zeiss) fitted with an environment chamber. Time-lapse images were acquired with a 40× NA1.3 oil objective and a camera (C9100-50; Hamamatsu Photonics) using Volocity software. 3D time-lapse images were acquired with a 63× NA1.4 oil objective and a camera (C11440-22CU; Hamamatsu Photonics) using Volocity software. Images were processed using Volocity or ImageJ software. For imaging in a single plane, cells were grown in eight-well coverglass chambers (LABTEK; Thermo Fisher Scientific) or glass-bottom Petri dishes (MatTek Corporation) to facilitate clearer imaging. For 3D imaging, cells were grown on Transwell filters or glass chambers coated with matrigel, and stacks of images were taken at different planes along the z axis for each time point. The imaging period began 20 min after the addition of POSs and continued for no more than 60 min. Cells were transfected with the following constructs: p*EGFPN1* (Takara Bio Inc.); pcDNA3-m*KLC1A-YFP* (provided by S. Encalada and L. Goldstein, University of California, San Diego, La Jolla, CA); p*TUBA1A-GFP* (OriGene); p*EGFPN-EB1* (provided by M. Seabra, Imperial College London, London, England, UK); or *pEGFPN-EB3* (provided by E. Colin and F. Perez, Institute Curie, Paris, France), using Lipofectamine LTX (Invitrogen) or Fugene HD (Roche). All constructs were sequenced to confirm identity before use.

Phagosome tracking analysis

Data on the trajectories of POS phagosomes were acquired and analyzed using Volocity software. Phagosomes were tracked for 3 min, and analysis was performed on those with a net displacement ≥2 µm and a diameter of 0.8–1.4 µm. Data were obtained from three WT and three *Klc1*$^{-/-}$ independent RPE primary cultures, grown in coverglass chambers. Definitions of tracking terms are as follows: track, the trajectory of a phagosome, covering a 3-min interval, and represented by its X and Y coordinate series; net displacement (in micrometer), distance between starting and ending points of a 3-min track; track segment, a period of uninterrupted movement, where the phagosome did not pause or change direction (by >135°); segmental speed (in micrometer/second), the distance of a track segment divided by the time taken; plus end segmental velocity (in micrometers/second), segmental velocity when the organelle is moving toward the periphery of the cell and away from the nucleus; minus end segmental velocity (in micrometers/second), segmental velocity when the organelle is moving toward the nucleus of the cell; reversal, direction changes by >135° and the displacement along the new direction is at least 1 µm; run length (in micrometers), the distance moved by a phagosome, without changing direction by >135°.

Statistical analyses were performed on Prism 4 (GraphPad), and one-tailed Mann–Whitney's test or paired Student's *t* test was used for phagosome tracking analysis.

In vivo retinal analysis

Light and EM. The posterior half of each eye was fixed by immersion in EM-grade 2% glutaraldehyde plus 2% formaldehyde (Electron Microscopy Sciences) in 0.1 M cacodylate buffer, postfixed in 1% OsO_4, and processed for embedment in epon-812. Photoreceptor cell counts were obtained from images of dorso-ventral semithin (0.7 mm) sections stained with toluidine blue. Regions that were 0.2-mm apart, beginning at the optic nerve head, were identified. In each region, at least three representative columns of photoreceptor cell nuclei were identified. When the photoreceptor nuclei line up in a column, it is a good indication that the retinal section is aligned vertically, and the vertical packing density of the nuclei is defined. The number of photoreceptor nuclei in each column was used to determine the thickness of the outer nuclear layer (ONL).

Ultrastructural analysis was performed with ultrathin sections (70 nm), stained with uranyl acetate and lead citrate, using regions of the retina, where the POSs were in complete longitudinal section.

Some retinas were processed by the OTAP postfixation method. After fixation with 2% glutaraldehyde plus 2% formaldehyde in 0.1 M cacodylate buffer, the tissues were postfixed with 1% OsO_4 in 0.1 M sodium cacodylate buffer (2.5 h), 1% tannic acid (30 min), 1% sodium $NaSO_4$ (5 min), 70% ethanol (three times for 5 min), and 1% paraphenylenediamine in 70% ethanol (30 min), and then processed for embedment in epon-812.

Microtubule decoration was performed according to a published procedure (Euteneuer and McIntosh, 1980; Troutt and Burnside, 1988). In brief, eyes were dissected into eyecups, and the sensory retina and the RPE/choroid was flat mounted and cut into 2-mm^2 pieces. Those pieces were incubated in permeabilization buffer with tubulin (0.5 M Pipes buffer, pH 6.9, 1 mM $MgCl_2$, 1 mM EGTA, 1 mM GTP, 1% Triton X-100, 0.5% deoxycolate, 0.2% SDS, 2.5% DMSO, and 1.8 mg/ml tubulin) at 0°C for 30 min (to prevent polymerization of tubulin during the initial permeabilization), followed by an incubation at RT for 15 min and then at 37°C for 15 min to promote free tubulin assembly into hooks. Tissue squares were then rinsed in 0.1 M cacodylate buffer and processed for EM as indicated previously. Microtubule polarity was assessed by the direction of curvature of hooks attached to microtubules in micrographs taken from sections perpendicular to the apical-basal axis of RPE cells, from the apical side toward the basal side. Hook curvature is directly related to microtubule polarity. A clockwise hook indicates that the observer is looking toward the minus end of

the microtubule, whereas a counterclockwise hook indicates that one is looking toward the plus end.

Sub-RPE deposits were quantified with sections representing at least four animals of each genotype (WT and mutant). For each animal, four images corresponding to the central region of the retina (within 1 mm of the optic nerve) were evaluated. The areas of the basal laminar deposits and the membranous debris were quantified relative to the length of the RPE spanning the analyzed areas.

For phagosome quantification, 70-nm dorso-ventral sections were collected from the region within 1.4 mm of the optic nerve. Phagosomes derived from outer segment shedding were identified by their characteristic structure (disk membrane presence). The adherens junctions were used to define the limit of the apical region of the RPE.

For light microscopy, we used a microscope (Axiophot; Carl Zeiss) with a 63× NA1.4 oil objective (Carl Zeiss) and a color camera (CoolSnap-Pro; Photometrics). Images were collected with Image-Pro Express software (Media Cybernetics).

For the EM and immunoEM study, we used a transmission electron microscope (EM910; Carl Zeiss) with a KeenView camera (Olympus), and images were collected with iTEM 5.0 software (Olympus).

For immunoEM, eyes were embedded in LR White (Electron Microscopy Sciences), and 70-nm sections were collected on grids and labeled, as described previously (Lopes et al., 2011). In brief, sections were blocked with 5% BSA in TBS-T, incubated with primary antibodies, followed by 12-nm conjugated secondary antibodies (Jackson ImmunoResearch Laboratories, Inc.), postfixed with 2% glutaraldehyde, and stained.

Statistical analysis was performed on Prism 5 (GraphPad), and two-tailed Student's *t* tests were used to test the probability of no significant difference between mutant and control samples.

Fluorescence microscopy. The posterior half of each eye from ∼P30 mice was fixed by immersion in 4% formaldehyde in PBS; washed in PBS; cryoprotected in 15, 20, and 30% sucrose solutions in PBS; and then embedded in OCT compound (Sakura). Dorso-ventral cryosections (10–12-µm thick) were blocked in 5% normal goat or donkey serum in PBS, incubated with primary antibody solutions overnight at 4°C, and then washed in PBS and stained with secondary antibodies for 1 h at RT in the dark. RPE flat mounts, or whole mounts of retinas from P30 mice, were fixed by immersion in 4% formaldehyde in PBS or in cold methanol, washed in PBS, and processed for immunolabeling as indicated previously. Alternatively, eyes were embedded in paraffin and processed and stained as described previously (Lopes et al., 2010).

The following primary antibodies were used: polyclonal rabbit anti-CTSD (provided by D. Bok, University of California, Los Angeles, Los Anegeles, CA; Bosch et al., 1993), anti-MDA (1:3,000; Abcam), anti–C5b-9 (1:100; Abcam), anti-fibronectin (1:200; Abcam), anti–β-tubulin (1:100; Cell Signaling Technology), anti-PARD3 (1:250; EMD Millipore), goat anti-C3d (1:50; R&D Systems), monoclonal rat anti-C3 (1:50; Hycult), mouse anti-acetylated tubulin (1:200; Sigma-Aldrich), anti–α-tubulin (1:200; Sigma-Aldrich), anti-Centrin3 (provided by U. Wolfrum, University of Mainz, Mainz, Germany), and anti-EB1 (1:100; BD). The secondary antibodies used were goat anti–rabbit, goat anti–mouse, donkey anti–goat, or donkey anti–rat IgG conjugated to Alexa Fluor 594 (Molecular Probes). Antibodies were prepared in 5% goat or donkey serum and 0.5% Triton X-100 in PBS. Sections were mounted using Fluorogel II with DAPI (Electron Microscopy Sciences) and analyzed on a confocal microscope (FluoView 1000; Olympus), with a 60× NA1.40 oil objective, using FluoView FV10-ASW 3.1 software (Olympus). Autofluorescence was detected using an excitation wavelength of 488 nm and an emission wavelength of 500–600 nm. Sections from control or mutant mice were imaged under identical conditions. Quantification of fluorescence levels was performed on gray-scale 16-bit TIFF images with ImageJ 1.43 software (National Institutes of Health). ImageJ was also used for stack projections and orthogonal projections. Statistical analysis was performed on Prism 5 (GraphPad), and two-tailed Student's *t* tests were used to test the probability of no significant difference between mutant and control samples.

STED super-resolution microscopy, using a confocal system (TCS SP5 STED; Leica) with an oil-immersion objective (HCX PL APO CS 100×/1.40 NA STED), was also performed on sections labeled with tubulin antibodies. In this case, the secondary antibody labeling was performed with goat anti–mouse IgG conjugated to ATTO647N (Active Motif) for 1 h at RT in the dark. Sections were mounted using ProLong Gold (Life Technologies). Leica Application Suite Advanced Fluorescence acquisition software was used.

Online supplemental material

The supplemental figures provide additional images of microtubule organization in the RPE (Fig. S1) and pathology in aged *Klc1*$^{-/-}$ mice (Fig. S3), and they show tracks of the phagosomes in each of three dimensions in WT RPE (Fig. S2). The videos show the following in RPE cells: the ingestion of POS phagosomes (Video 1), the movement of POS phagosomes along labeled microtubules (Video 2), the association of KLC1-YFP with motile phagosomes (Video 3), and two examples of the tracking of POS phagosomes (Videos 4 and 5). Online supplemental material is available at http://www.jcb.org/cgi/content/full/jcb.201410112/DC1.

Acknowledgments

We are grateful to Sandra Encalada and Larry Goldstein for providing the plasmids pcDNA3-m*KLC1A-YFP*, for providing some mouse tissues, and for helpful discussions. We thank Miguel Seabra for the p*EGFP*-N-*EB1* plasmid; Emilie Colin and Franck Perez for the p*EGFP-EB3* plasmid; Dean Bok for the CTSD antibody; Juyea Hoo for help with sample preparation and sectioning for light microscopy; and Samer Habib, Paul Kim, and Steven Nusinowitz for their help in attempting OCT and ERG analysis.

STED microscopy was performed at the California NanoSystems Institute Advanced Light Microscopy/Spectroscopy Shared Resource Facility at UCLA, supported in part by funding from a National Science Foundation Major Research Instrumentation grant (CHE-0722519); we thank Laurent Bentolila for assistance. The research was supported by National Institutes of Health (NIH) R01 grants EY13408 and EY07042, NIH core grant EY00331, and an RPB Jules and Doris Stein Professorship (to D.S. Williams).

The authors declare no competing financial interests.

Submitted: 28 October 2014
Accepted: 2 July 2015

References

Al-Haddad, A., M.A. Shonn, B. Redlich, A. Blocker, J.K. Burkhardt, H. Yu, J.A. Hammer III, D.G. Weiss, W. Steffen, G. Griffiths, and S.A. Kuznetsov. 2001. Myosin Va bound to phagosomes binds to F-actin and delays microtubule-dependent motility. *Mol. Biol. Cell.* 12:2742–2755. http://dx.doi.org/10.1091/mbc.12.9.2742

Anderson, D.H., M.J. Radeke, N.B. Gallo, E.A. Chapin, P.T. Johnson, C.R. Curletti, L.S. Hancox, J. Hu, J.N. Ebright, G. Malek, et al. 2010. The pivotal role of the complement system in aging and age-related macular degeneration: Hypothesis re-visited. *Prog. Retin. Eye Res.* 29:95–112. http://dx.doi.org/10.1016/j.preteyeres.2009.11.003

Andersson, M.E., M. Zetterberg, G. Tasa, M. Seibt-Palmér, E. Juronen, P. Teesalu, K. Blennow, and H. Zetterberg. 2007. Variability in the kinesin light chain 1 gene may influence risk of age-related cataract. *Mol. Vis.* 13:993–996.

Atwood, S.X., M. Li, A. Lee, J.Y. Tang, and A.E. Oro. 2013. GLI activation by atypical protein kinase C ι/λ regulates the growth of basal cell carcinomas. *Nature.* 494:484–488. http://dx.doi.org/10.1038/nature11889

Bacallao, R., C. Antony, C. Dotti, E. Karsenti, E.H. Stelzer, and K. Simons. 1989. The subcellular organization of Madin-Darby canine kidney cells during the formation of a polarized epithelium. *J. Cell Biol.* 109:2817–2832. http://dx.doi.org/10.1083/jcb.109.6.2817

Blocker, A., F.F. Severin, A. Habermann, A.A. Hyman, G. Griffiths, and J.K. Burkhardt. 1996. Microtubule-associated protein-dependent binding of phagosomes to microtubules. *J. Biol. Chem.* 271:3803–3811. http://dx.doi.org/10.1074/jbc.271.7.3803

Blocker, A., F.F. Severin, J.K. Burkhardt, J.B. Bingham, H. Yu, J.C. Olivo, T.A. Schroer, A.A. Hyman, and G. Griffiths. 1997. Molecular requirements for bi-directional movement of phagosomes along microtubules. *J. Cell Biol.* 137:113–129. http://dx.doi.org/10.1083/jcb.137.1.113

Blocker, A., G. Griffiths, J.C. Olivo, A.A. Hyman, and F.F. Severin. 1998. A role for microtubule dynamics in phagosome movement. *J. Cell Sci.* 111:303–312.

Bosch, E., J. Horwitz, and D. Bok. 1993. Phagocytosis of outer segments by retinal pigment epithelium: phagosome-lysosome interaction. *J. Histochem. Cytochem.* 41:253–263. http://dx.doi.org/10.1177/41.2.8419462

Bowes Rickman, C., S. Farsiu, C.A. Toth, and M. Klingeborn. 2013. Dry age-related macular degeneration: Mechanisms, therapeutic targets, and imaging. *Invest. Ophthalmol. Vis. Sci.* 54:ORSF68–ORSF80. http://dx.doi.org/10.1167/iovs.13-12757

Curcio, C.A., J.B. Presley, C.L. Millican, and N.E. Medeiros. 2005. Basal deposits and drusen in eyes with age-related maculopathy: evidence for solid lipid particles. *Exp. Eye Res.* 80:761–775. http://dx.doi.org/10.1016/j.exer.2004.09.017

Curcio, C.A., J.D. Messinger, K.R. Sloan, G. McGwin, N.E. Medeiros, and R.F. Spaide. 2013. Subretinal drusenoid deposits in non-neovascular age-related macular degeneration: Morphology, prevalence, topography, and biogenesis model. *Retina.* 33:265–276. http://dx.doi.org/10.1097/IAE.0b013e31827e25e0

Desjardins, M., L.A. Huber, R.G. Parton, and G. Griffiths. 1994. Biogenesis of phagolysosomes proceeds through a sequential series of interactions with the endocytic apparatus. *J. Cell Biol.* 124:677–688. http://dx.doi.org/10.1083/jcb.124.5.677

Diemer, T., D. Gibbs, and D.S. Williams. 2008. Analysis of the rate of disk membrane digestion by cultured RPE cells. *Adv. Exp. Med. Biol.* 613:321–326. http://dx.doi.org/10.1007/978-0-387-74904-4_37

Encalada, S.E., L. Szpankowski, C.H. Xia, and L.S. Goldstein. 2011. Stable kinesin and dynein assemblies drive the axonal transport of mammalian prion protein vesicles. *Cell.* 144:551–565. http://dx.doi.org/10.1016/j.cell.2011.01.021

Esteve-Rudd, J., V.S. Lopes, M. Jiang, and D.S. Williams. 2014. In vivo and in vitro monitoring of phagosome maturation in retinal pigment epithelium cells. *Adv. Exp. Med. Biol.* 801:85–90. http://dx.doi.org/10.1007/978-1-4614-3209-8_11

Euteneuer, U., and J.R. McIntosh. 1980. Polarity of midbody and phragmoplast microtubules. *J. Cell Biol.* 87:509–515. http://dx.doi.org/10.1083/jcb.87.2.509

Fan, S., T.W. Hurd, C.J. Liu, S.W. Straight, T. Weimbs, E.A. Hurd, S.E. Domino, and B. Margolis. 2004. Polarity proteins control ciliogenesis via kinesin motor interactions. *Curr. Biol.* 14:1451–1461. http://dx.doi.org/10.1016/j.cub.2004.08.025

Feeney, L. 1973. The phagolysosomal system of the pigment epithelium. A key to retinal disease. *Invest. Ophthalmol.* 12:635–638.

Feeney-Burns, L., and G.E. Eldred. 1983. The fate of the phagosome: conversion to 'age pigment' and impact in human retinal pigment epithelium. *Trans. Ophthalmol. Soc. U. K.* 103:416–421.

Finnemann, S.C., L.W. Leung, and E. Rodriguez-Boulan. 2002. The lipofuscin component A2E selectively inhibits phagolysosomal degradation of photoreceptor phospholipid by the retinal pigment epithelium. *Proc. Natl. Acad. Sci. USA.* 99:3842–3847. http://dx.doi.org/10.1073/pnas.052025899

Friedman, D.S., and R.D. Vale. 1999. Single-molecule analysis of kinesin motility reveals regulation by the cargo-binding tail domain. *Nat. Cell Biol.* 1:293–297. http://dx.doi.org/10.1038/13008

Frost, L.S., V.S. Lopes, A. Bragin, J. Reyes-Reveles, J. Brancato, A. Cohen, C.H. Mitchell, D.S. Williams, and K. Boesze-Battaglia. 2014. The contribution of melanoregulin to microtubule-associated protein 1 light chain 3 (LC3) associated phagocytosis in retinal pigment epithelium. *Mol. Neurobiol.* In press. http://dx.doi.org/10.1007/s12035-014-8920-5

Fu, M.M., and E.L. Holzbaur. 2013. JIP1 regulates the directionality of APP axonal transport by coordinating kinesin and dynein motors. *J. Cell Biol.* 202:495–508. http://dx.doi.org/10.1083/jcb.201302078

Fu, M.M., and E.L. Holzbaur. 2014. Integrated regulation of motor-driven organelle transport by scaffolding proteins. *Trends Cell Biol.* 24:564–574. http://dx.doi.org/10.1016/j.tcb.2014.05.002

Fu, M.M., J.J. Nirschl, and E.L. Holzbaur. 2014. LC3 binding to the scaffolding protein JIP1 regulates processive dynein-driven transport of autophagosomes. *Dev. Cell.* 29:577–590. http://dx.doi.org/10.1016/j.devcel.2014.04.015

Futter, C.E., J.S. Ramalho, G.B. Jaissle, M.W. Seeliger, and M.C. Seabra. 2004. The role of Rab27a in the regulation of melanosome distribution within retinal pigment epithelial cells. *Mol. Biol. Cell.* 15:2264–2275. http://dx.doi.org/10.1091/mbc.E03-10-0772

Gibbs, D., and D.S. Williams. 2003. Isolation and culture of primary mouse retinal pigmented epithelial cells. *Adv. Exp. Med. Biol.* 533:347–352. http://dx.doi.org/10.1007/978-1-4615-0067-4_44

Gibbs, D., J. Kitamoto, and D.S. Williams. 2003. Abnormal phagocytosis by retinal pigmented epithelium that lacks myosin VIIa, the Usher syndrome 1B protein. *Proc. Natl. Acad. Sci. USA.* 100:6481–6486. http://dx.doi.org/10.1073/pnas.1130432100

Gibbs, D., S.M. Azarian, C. Lillo, J. Kitamoto, A.E. Klomp, K.P. Steel, R.T. Libby, and D.S. Williams. 2004. Role of myosin VIIa and Rab27a in the motility and localization of RPE melanosomes. *J. Cell Sci.* 117:6473–6483. http://dx.doi.org/10.1242/jcs.01580

Gilbert, T., A. Le Bivic, A. Quaroni, and E. Rodriguez-Boulan. 1991. Microtubular organization and its involvement in the biogenetic pathways of plasma membrane proteins in Caco-2 intestinal epithelial cells. *J. Cell Biol.* 113:275–288. http://dx.doi.org/10.1083/jcb.113.2.275

Gordiyenko, N.V., R.N. Fariss, C. Zhi, and I.M. MacDonald. 2010. Silencing of the CHM gene alters phagocytic and secretory pathways in the retinal pigment epithelium. *Invest. Ophthalmol. Vis. Sci.* 51:1143–1150. http://dx.doi.org/10.1167/iovs.09-4117

Guyton, J.R., and K.F. Klemp. 1988. Ultrastructural discrimination of lipid droplets and vesicles in atherosclerosis: value of osmium-thiocarbohydrazide-osmium and tannic acid-paraphenylenediamine techniques. *J. Histochem. Cytochem.* 36:1319–1328. http://dx.doi.org/10.1177/36.10.2458408

Hendricks, A.G., E. Perlson, J.L. Ross, H.W. Schroeder III, M. Tokito, and E.L. Holzbaur. 2010. Motor coordination via a tug-of-war mechanism drives bidirectional vesicle transport. *Curr. Biol.* 20:697–702. http://dx.doi.org/10.1016/j.cub.2010.02.058

Herman, K.G., and R.H. Steinberg. 1982. Phagosome movement and the diurnal pattern of phagocytosis in the tapetal retinal pigment epithelium of the opossum. *Invest. Ophthalmol. Vis. Sci.* 23:277–290.

Hogan, M.J. 1972. Role of the retinal pigment epithelium in macular disease. *Trans. Am. Acad. Ophthalmol. Otolaryngol.* 76:64–80.

Hollyfield, J.G., V.L. Bonilha, M.E. Rayborn, X. Yang, K.G. Shadrach, L. Lu, R.L. Ufret, R.G. Salomon, and V.L. Perez. 2008. Oxidative damage-induced inflammation initiates age-related macular degeneration. *Nat. Med.* 14:194–198. http://dx.doi.org/10.1038/nm1709

Hosein, R.E., S.A. Williams, and R.H. Gavin. 2005. Directed motility of phagosomes in *Tetrahymena thermophila* requires actin and Myo1p, a novel unconventional myosin. *Cell Motil. Cytoskeleton.* 61:49–60. http://dx.doi.org/10.1002/cm.20065

Imamura, Y., S. Noda, K. Hashizume, K. Shinoda, M. Yamaguchi, S. Uchiyama, T. Shimizu, Y. Mizushima, T. Shirasawa, and K. Tsubota. 2006. Drusen, choroidal neovascularization, and retinal pigment epithelium dysfunction in SOD1-deficient mice: A model of age-related macular degeneration. *Proc. Natl. Acad. Sci. USA.* 103:11282–11287. http://dx.doi.org/10.1073/pnas.0602131103

Justilien, V., J.J. Pang, K. Renganathan, X. Zhan, J.W. Crabb, S.R. Kim, J.R. Sparrow, W.W. Hauswirth, and A.S. Lewin. 2007. SOD2 knockdown mouse model of early AMD. *Invest. Ophthalmol. Vis. Sci.* 48:4407–4420. http://dx.doi.org/10.1167/iovs.07-0432

Kim, J.Y., H. Zhao, J. Martinez, T.A. Doggett, A.V. Kolesnikov, P.H. Tang, Z. Ablonczy, C.C. Chan, Z. Zhou, D.R. Green, and T.A. Ferguson. 2013. Noncanonical autophagy promotes the visual cycle. *Cell.* 154:365–376. http://dx.doi.org/10.1016/j.cell.2013.06.012

Krock, B.L., J. Bilotta, and B.D. Perkins. 2007. Noncell-autonomous photoreceptor degeneration in a zebrafish model of choroideremia. *Proc. Natl. Acad. Sci. USA.* 104:4600–4605. http://dx.doi.org/10.1073/pnas.0605818104

LaVail, M.M. 1976. Rod outer segment disk shedding in rat retina: relationship to cyclic lighting. *Science.* 194:1071–1074. http://dx.doi.org/10.1126/science.982063

Lehmann, G.L., I. Benedicto, N.J. Philp, and E. Rodriguez-Boulan. 2014. Plasma membrane protein polarity and trafficking in RPE cells: Past, present and future. *Exp. Eye Res.* 126:5–15. http://dx.doi.org/10.1016/j.exer.2014.04.021

Liu, X., G. Vansant, I.P. Udovichenko, U. Wolfrum, and D.S. Williams. 1997. Myosin VIIa, the product of the Usher 1B syndrome gene, is concentrated in the connecting cilia of photoreceptor cells. *Cell Motil. Cytoskeleton.* 37:240–252. http://dx.doi.org/10.1002/(SICI)1097-0169(1997)37:3<240::AID-CM6>3.0.CO;2-A

Liu, X., I.P. Udovichenko, S.D.M. Brown, K.P. Steel, and D.S. Williams. 1999. Myosin VIIa participates in opsin transport through the photoreceptor cilium. *J. Neurosci.* 19:6267–6274.

Lopes, V.S., J.S. Ramalho, D.M. Owen, M.O. Karl, O. Strauss, C.E. Futter, and M.C. Seabra. 2007. The ternary Rab27a-Myrip-Myosin VIIa complex regulates melanosome motility in the retinal pigment epithelium. *Traffic.* 8:486–499. http://dx.doi.org/10.1111/j.1600-0854.2007.00548.x

Lopes, V.S., D. Jimeno, K. Khanobdee, X. Song, B. Chen, S. Nusinowitz, and D.S. Williams. 2010. Dysfunction of heterotrimeric kinesin-2 in rod photoreceptor cells and the role of opsin mislocalization in rapid cell death. *Mol. Biol. Cell.* 21:4076–4088. http://dx.doi.org/10.1091/mbc.E10-08-0715

Lopes, V.S., D. Gibbs, R.T. Libby, T.S. Aleman, D.L. Welch, C. Lillo, S.G. Jacobson, R.A. Radu, K.P. Steel, and D.S. Williams. 2011. The Usher 1B protein, MYO7A, is required for normal localization and function of the visual retinoid cycle enzyme, RPE65. *Hum. Mol. Genet.* 20:2560–2570. http://dx.doi.org/10.1093/hmg/ddr155

Luhmann, U.F., L.S. Carvalho, S.M. Holthaus, J.A. Cowing, S. Greenaway, C.J. Chu, P. Herrmann, A.J. Smith, P.M. Munro, P. Potter, et al. 2015. The severity of retinal pathology in homozygous Crb1rd8/rd8 mice is dependent on additional genetic factors. *Hum. Mol. Genet.* 24:128–141. http://dx.doi.org/10.1093/hmg/ddu424

Maday, S., K.E. Wallace, and E.L. Holzbaur. 2012. Autophagosomes initiate distally and mature during transport toward the cell soma in primary neurons. *J. Cell Biol.* 196:407–417. http://dx.doi.org/10.1083/jcb.201106120

Marshall, G.E., A.G. Konstas, G.G. Reid, J.G. Edwards, and W.R. Lee. 1992. Type IV collagen and laminin in Bruch's membrane and basal linear deposit in the human macula. *Br. J. Ophthalmol.* 76:607–614. http://dx.doi.org/10.1136/bjo.76.10.607

Mattapallil, M.J., E.F. Wawrousek, C.C. Chan, H. Zhao, J. Roychoudhury, T.A. Ferguson, and R.R. Caspi. 2012. The Rd8 mutation of the Crb1 gene is present in vendor lines of C57BL/6N mice and embryonic stem cells, and confounds ocular induced mutant phenotypes. *Invest. Ophthalmol. Vis. Sci.* 53:2921–2927. http://dx.doi.org/10.1167/iovs.12-9662

Mazzoni, F., H. Safa, and S.C. Finnemann. 2014. Understanding photoreceptor outer segment phagocytosis: Use and utility of RPE cells in culture. *Exp. Eye Res.* 126:51–60. http://dx.doi.org/10.1016/j.exer.2014.01.010

Müller, M.J., S. Klumpp, and R. Lipowsky. 2008. Tug-of-war as a cooperative mechanism for bidirectional cargo transport by molecular motors. *Proc. Natl. Acad. Sci. USA.* 105:4609–4614. http://dx.doi.org/10.1073/pnas.0706825105

Nishiyama, K., H. Sakaguchi, J.G. Hu, D. Bok, and J.G. Hollyfield. 2002. Claudin localization in cilia of the retinal pigment epithelium. *Anat. Rec.* 267:196–203. http://dx.doi.org/10.1002/ar.10102

Osterberg, G.A. 1935. Topography of the layer of rods and cones in the human retina. *Acta Ophthalmol. (Copenh.).* 6:1–10.

Pernigo, S., A. Lamprecht, R.A. Steiner, and M.P. Dodding. 2013. Structural basis for kinesin-1:cargo recognition. *Science.* 340:356–359. http://dx.doi.org/10.1126/science.1234264

Pikuleva, I.A., and C.A. Curcio. 2014. Cholesterol in the retina: The best is yet to come. *Prog. Retin. Eye Res.* 41:64–89. http://dx.doi.org/10.1016/j.preteyeres.2014.03.002

Rabinowitz, S., H. Horstmann, S. Gordon, and G. Griffiths. 1992. Immunocytochemical characterization of the endocytic and phagolysosomal compartments in peritoneal macrophages. *J. Cell Biol.* 116:95–112. http://dx.doi.org/10.1083/jcb.116.1.95

Rahman, A., D.S. Friedman, and L.S. Goldstein. 1998. Two kinesin light chain genes in mice. Identification and characterization of the encoded proteins. *J. Biol. Chem.* 273:15395–15403. http://dx.doi.org/10.1074/jbc.273.25.15395

Rahman, A., A. Kamal, E.A. Roberts, and L.S. Goldstein. 1999. Defective kinesin heavy chain behavior in mouse kinesin light chain mutants. *J. Cell Biol.* 146:1277–1288. http://dx.doi.org/10.1083/jcb.146.6.1277

Rakoczy, P.E., D. Zhang, T. Robertson, N.L. Barnett, J. Papadimitriou, I.J. Constable, and C.M. Lai. 2002. Progressive age-related changes similar to age-related macular degeneration in a transgenic mouse model. *Am. J. Pathol.* 161:1515–1524. http://dx.doi.org/10.1016/S0002-9440(10)64427-6

Regan, C.M., W.J. de Grip, F.J. Daemen, and S.L. Bonting. 1980. Degradation of rhodopsin by a lysosomal fraction of retinal pigment epithelium: Biochemical aspects of the visual process. XLI. *Exp. Eye Res.* 30:183–191. http://dx.doi.org/10.1016/0014-4835(80)90112-8

Reis, G.F., G. Yang, L. Szpankowski, C. Weaver, S.B. Shah, J.T. Robinson, T.S. Hays, G. Danuser, and L.S. Goldstein. 2012. Molecular motor function in axonal transport in vivo probed by genetic and computational analysis in Drosophila. *Mol. Biol. Cell.* 23:1700–1714. http://dx.doi.org/10.1091/mbc.E11-11-0938

Rizzolo, L.J., and H.C. Joshi. 1993. Apical orientation of the microtubule organizing center and associated gamma-tubulin during the polarization of the retinal pigment epithelium in vivo. *Dev. Biol.* 157:147–156. http://dx.doi.org/10.1006/dbio.1993.1119

Saxton, W.M., and P.J. Hollenbeck. 2012. The axonal transport of mitochondria. *J. Cell Sci.* 125:2095–2104. http://dx.doi.org/10.1242/jcs.053850

Seabra, M.C., M.S. Brown, and J.L. Goldstein. 1993. Retinal degeneration in choroideremia: deficiency of rab geranylgeranyl transferase. *Science.* 259:377–381. http://dx.doi.org/10.1126/science.8380507

Seabra, M.C., Y.K. Ho, and J.S. Anant. 1995. Deficient geranylgeranylation of Ram/Rab27 in choroideremia. *J. Biol. Chem.* 270:24420–24427. http://dx.doi.org/10.1074/jbc.270.41.24420

Shaw, P.X., L. Zhang, M. Zhang, H. Du, L. Zhao, C. Lee, S. Grob, S.L. Lim, G. Hughes, J. Lee, et al. 2012. Complement factor H genotypes impact risk of age-related macular degeneration by interaction with oxidized phospholipids. *Proc. Natl. Acad. Sci. USA.* 109:13757–13762. http://dx.doi.org/10.1073/pnas.1121309109

Soppina, V., A.K. Rai, A.J. Ramaiya, P. Barak, and R. Mallik. 2009. Tug-of-war between dissimilar teams of microtubule motors regulates transport and fission of endosomes. *Proc. Natl. Acad. Sci. USA.* 106:19381–19386. http://dx.doi.org/10.1073/pnas.0906524106

Sparrow, J.R., and M. Boulton. 2005. RPE lipofuscin and its role in retinal pathobiology. *Exp. Eye Res.* 80:595–606. http://dx.doi.org/10.1016/j.exer.2005.01.007

Sparrow, J.R., E. Gregory-Roberts, K. Yamamoto, A. Blonska, S.K. Ghosh, K. Ueda, and J. Zhou. 2012. The bisretinoids of retinal pigment epithelium. *Prog. Retin. Eye Res.* 31:121–135. http://dx.doi.org/10.1016/j.preteyeres.2011.12.001

Stokin, G.B., C. Lillo, T.L. Falzone, R.G. Brusch, E. Rockenstein, S.L. Mount, R. Raman, P. Davies, E. Masliah, D.S. Williams, and L.S. Goldstein. 2005. Axonopathy and transport deficits early in the pathogenesis of Alzheimer's disease. *Science.* 307:1282–1288. http://dx.doi.org/10.1126/science.1105681

Strunnikova, N.V., A. Maminishkis, J.J. Barb, F. Wang, C. Zhi, Y. Sergeev, W. Chen, A.O. Edwards, D. Stambolian, G. Abecasis, et al. 2010. Transcriptome analysis and molecular signature of human retinal pigment epithelium. *Hum. Mol. Genet.* 19:2468–2486. http://dx.doi.org/10.1093/hmg/ddq129

Troutt, L.L., and B. Burnside. 1988. The unusual microtubule polarity in teleost retinal pigment epithelial cells. *J. Cell Biol.* 107:1461–1464. http://dx.doi.org/10.1083/jcb.107.4.1461

Tsang, S.H., M.E. Burns, P.D. Calvert, P. Gouras, D.A. Baylor, S.P. Goff, and V.Y. Arshavsky. 1998. Role for the target enzyme in deactivation of photoreceptor G protein in vivo. *Science.* 282:117–121. http://dx.doi.org/10.1126/science.282.5386.117

Tuma, M.C., A. Zill, N. Le Bot, I. Vernos, and V. Gelfand. 1998. Heterotrimeric kinesin II is the microtubule motor protein responsible for pigment dispersion in *Xenopus* melanophores. *J. Cell Biol.* 143:1547–1558. http://dx.doi.org/10.1083/jcb.143.6.1547

Udovichenko, I.P., D. Gibbs, and D.S. Williams. 2002. Actin-based motor properties of native myosin VIIa. *J. Cell Sci.* 115:445–450.

Ufret-Vincenty, R.L., B. Aredo, X. Liu, A. McMahon, P.W. Chen, H. Sun, J.Y. Niederkorn, and W. Kedzierski. 2010. Transgenic mice expressing variants of complement factor H develop AMD-like retinal findings. *Invest. Ophthalmol. Vis. Sci.* 51:5878–5887. http://dx.doi.org/10.1167/iovs.09-4457

Verhey, K.J., D.L. Lizotte, T. Abramson, L. Barenboim, B.J. Schnapp, and T.A. Rapoport. 1998. Light chain–dependent regulation of Kinesin's interaction with microtubules. *J. Cell Biol.* 143:1053–1066. http://dx.doi.org/10.1083/jcb.143.4.1053

Verhey, K.J., D. Meyer, R. Deehan, J. Blenis, B.J. Schnapp, T.A. Rapoport, and B. Margolis. 2001. Cargo of kinesin identified as JIP scaffolding proteins and associated signaling molecules. *J. Cell Biol.* 152:959–970. http://dx.doi.org/10.1083/jcb.152.5.959

Volland, S., J. Esteve-Rudd, J. Hoo, C. Yee, and D.S. Williams. 2015. A comparison of some organizational characteristics of the mouse central retina and the human macula. *PLoS ONE.* 10:e0125631. http://dx.doi.org/10.1371/journal.pone.0125631

Wavre-Shapton, S.T., T. Tolmachova, M. Lopes da Silva, C.E. Futter, and M.C. Seabra. 2013. Conditional ablation of the choroideremia gene causes age-related changes in mouse retinal pigment epithelium. *PLoS ONE.* 8:e57769. http://dx.doi.org/10.1371/journal.pone.0057769

Wavre-Shapton, S.T., I.P. Meschede, M.C. Seabra, and C.E. Futter. 2014. Phagosome maturation during endosome interaction revealed by partial rhodopsin processing in retinal pigment epithelium. *J. Cell Sci.* 127:3852–3861. http://dx.doi.org/10.1242/jcs.154757

Weil, D., S. Blanchard, J. Kaplan, P. Guilford, F. Gibson, J. Walsh, P. Mburu, A. Varela, J. Levilliers, M.D. Weston, et al. 1995. Defective myosin VIIA gene responsible for Usher syndrome type 1B. *Nature.* 374:60–61. http://dx.doi.org/10.1038/374060a0

Weismann, D., K. Hartvigsen, N. Lauer, K.L. Bennett, H.P. Scholl, P. Charbel Issa, M. Cano, H. Brandstätter, S. Tsimikas, C. Skerka, et al. 2011. Complement factor H binds malondialdehyde epitopes and protects from oxidative stress. *Nature.* 478:76–81. http://dx.doi.org/10.1038/nature10449

Welte, M.A. 2004. Bidirectional transport along microtubules. *Curr. Biol.* 14:R525–R537. http://dx.doi.org/10.1016/j.cub.2004.06.045

Williams, D.S. 2008. Usher syndrome: Animal models, retinal function of Usher proteins, and prospects for gene therapy. *Vision Res.* 48:433–441. http://dx.doi.org/10.1016/j.visres.2007.08.015

Wu, X., B. Bowers, K. Rao, Q. Wei, and J.A. Hammer III. 1998. Visualization of melanosome dynamics within wild-type and dilute melanocytes suggests a paradigm for myosin V function in vivo. *J. Cell Biol.* 143:1899–1918. http://dx.doi.org/10.1083/jcb.143.7.1899

Young, R.W. 1967. The renewal of photoreceptor cell outer segments. *J. Cell Biol.* 33:61–72. http://dx.doi.org/10.1083/jcb.33.1.61

Young, R.W., and D. Bok. 1969. Participation of the retinal pigment epithelium in the rod outer segment renewal process. *J. Cell Biol.* 42:392–403. http://dx.doi.org/10.1083/jcb.42.2.392

Zhang, L., J.W. Xu, X. Qu, D.R. Liu, P. Liu, and X.Z. Zhao. 2013. Association of a rare haplotype in Kinesin light chain 1 gene with age-related cataract in a Han Chinese population. *PLoS ONE.* 8:e64052. http://dx.doi.org/10.1371/journal.pone.0064052